



M-band flexible wavelet transform and its application to the fault diagnosis of planetary gear transmission systems

Yi Qin ^{a,*}, Yongfang Mao ^a, Baoping Tang ^a, Yi Wang ^a, Haizhou Chen ^b

^aState Key Laboratory of Mechanical Transmission, Chongqing University, Chongqing 400044, People's Republic of China

^bCollege of Electromechanical Engineering, Qingdao University of Science and Technology, Laoshan District, Qingdao 266061, People's Republic of China



ARTICLE INFO

Article history:

Received 30 June 2018

Received in revised form 1 June 2019

Accepted 8 August 2019

Keywords:

Planetary gear transmission systems

Filter bank design

Tunable sampling factor

Weak transient feature

Incipient fault detection

ABSTRACT

The fault diagnosis of planetary gear transmission systems is crucial for the safety of machineries and equipment. To identify the underlying fault features in measured signals, a novel M-band flexible wavelet transform is constructed. This transform provides a denser sampling of the time-frequency plane and preserves tunable filter parameters and dilation factors. A perfect reconstruction condition of the proposed transform is established, and its corresponding wavelet filter bank is designed to satisfy the perfect reconstruction condition. A numerical implementation algorithm of M-band flexible wavelet transform is investigated using a multirate filter bank and fast Fourier transform. Denoising the simulation signals demonstrates that the proposed transform exhibits better performance than analytic flexible wavelet transform, orthogonal wavelet transform, and biorthogonal wavelet transform. A new fault diagnosis method for planetary gear transmission systems is proposed on the basis of M-band flexible wavelet transform and spectral negentropy. Experimental and comparative results show that the proposed method can be more effectively and accurately applied to the fault diagnosis of planetary gear transmission systems compared with typical fault diagnosis methods based on analytic flexible wavelet transform, Morlet wavelet transform, and infograms.

© 2019 Elsevier Ltd. All rights reserved.

1. Introduction

Gear transmission systems play important roles in rotating machineries. Compared with conventional fixed-shaft gear transmission, planetary gear transmission has a more compact structure, higher transmission ratio, and higher efficiency even under heavy loads; thus, it has gained wide applications in several important machines, such as helicopters, automobiles, ships, excavators, wind turbines, and heavy trucks [1]. However, planetary gear transmission systems generally run under severe working and environmental conditions, and thus, their gears are vulnerable to various faults, such as fatigue cracks, pitting, and broken teeth. These faults may lead to the shutdown of an entire transmission train and even to economic or life losses. Consequently, the fault diagnosis of planetary gear transmission systems is crucial for reducing downtime and preventing accidents. Various methods have been proposed to detect gear transmission faults; these methods include vibration, acoustic emission, sound, temperature, and wear debris analyses [2]. Among these methods, vibration analysis is the most widely used because vibration signals can effectively reflect the dynamic behavior of gear transmission systems and

* Corresponding author.

E-mail address: qy_808@aliyun.com (Y. Qin).

contain a considerable amount of fault information. In the current study, we focus on a vibration-based fault diagnosis method for planetary gear transmission systems.

The actual test conditions and the dynamics analysis of a faulty planetary gearbox [3,4] indicate that the measured vibration signal is complex and includes various frequency contents, such as amplitude modulation and frequency modulation components, transient components, harmonic components, and noise. The fault feature generated by the damaged gear is probably submerged in other normal vibrations and noises. Thus, numerous signal processing methods have been developed to extract fault features from the vibration signals of planetary gear transmission systems. For example, the time synchronous averaging method was applied to denoise the vibration signals of gearboxes [5]. Complex Morlet wavelets were used to extract the fault feature of a helicopter's planetary gearbox [6]. Dense framelets were constructed to remove noise within the vibration signals of gearboxes and enhance the transient feature [7]. To reduce the path transfer effect, a simple frequency-domain algorithm was explored for the early detection of damaged gears [8]. A modified sideband energy ratio was proposed to diagnose the faults of planetary gear transmission systems under speed fluctuations [9]. A fault diagnosis method based on iterative generalized demodulation and time-frequency reassignment was proposed for extracting the time-varying fault features of planetary gear transmission systems [10]. A joint amplitude and frequency demodulation method was applied to diagnose a faulty planetary gearbox via ensemble empirical mode decomposition and an energy separation algorithm [11]. A time-frequency analysis approach based on the Vold-Kalman filter and higher-order energy separation was proposed for the fault diagnosis of wind turbine planetary gearboxes under nonstationary conditions [12]. An order tracking method based on a discrete spectrum correction technique was developed for processing the nonstationary vibration signals of wind turbine planetary gear transmission systems [13]. A transient feature identification method based on sparse representation was proposed to detect the fault of a wind turbine planetary gearbox [14]. An adaptive iterative thresholding algorithm with improved kurtosis was developed to extract the fault features of planetary gear transmission systems [15]. A fault diagnosis method for planetary gear transmission systems based on an adaptive multiscale morphological filter, modified hierarchical permutation entropy, and a binary tree support vector machine was proposed to identify various gear faults [16]. A scheme based on modified multiscale symbolic dynamic entropy and minimum redundancy maximum relevance feature selection was designed to diagnose the faults of planetary gear transmission systems by the same research group [17]. The spectral kurtosis method was applied to detect gear tooth cracks in a wind turbine planetary gearbox [18]. Other typical fault diagnosis methods for planetary gear transmission systems are provided in [19–27].

From the preceding studies, fault diagnosis methods for planetary gear transmission systems are classified into time-domain analysis, frequency-domain analysis, wavelet transform, signal decomposition, filtering based on a characteristic index, and entropy-based methods. Among these methods, wavelet transform is extremely suitable for processing the low signal-to-noise ratio vibration signals of planetary gear transmission systems due to its fine time-frequency localization property and the outstanding performance of weak information "zoom-in." Traditional discrete wavelet transform (DWT) has been widely applied to various signal processing tasks. To increase the computation speed of biorthogonal DWT, lifting wavelet transform was proposed by Sweldens [28], and its improvement, namely, constrained adaptive lifting wavelet transform, was successfully applied to detecting the fault of a helicopter's planetary transmission system [29]. Customized multiwavelets were constructed via a redundant lifting scheme and used to detect impulses caused by the fault of a planetary gearbox [30]. DWT has a low time-frequency resolution and lacks symmetry; thus, various overcomplete wavelet transforms were proposed to obtain desirable properties, such as smoothness, shift invariance, symmetry, high approximation orders, and dense time-frequency sampling. [31–33]. A higher-density dyadic wavelet transform with strict shift invariance was developed to extract gearbox fault feature [34]. To further increase frequency resolution, rational dilation wavelet transform [35] and overcomplete rational dilation wavelet transform [36] were proposed; the latter was effectively applied to diagnosing gearbox fault [37]. However, the sampling rates of these transforms are difficult to adjust to specific situations. Therefore, an analytic wavelet transform with dilation and shift parameters that can be easily customized was explored [38] and successfully used to extract the weak fault feature of a planetary gearbox [39]. However, analytic wavelet transform only divides the frequency band into two sub-bands (low-frequency and high-frequency sub-bands) in each stage, i.e., its filter bank only consists of a low-pass filter and a high-pass filter. Evidently, the sampling density of a time-frequency plane can be increased further by adding more filtering channels, and the underlying fault feature of the planetary gearbox can be more effectively detected. Driven by these motivations, we propose a novel M-band flexible wavelet transform with a filter bank composed of a low-pass filter, a band-pass filter, and a high-pass filter. $M = 2$ for such a filter bank, and $M = 1$ for analytic wavelet transform. A perfect reconstruction condition for M-band flexible wavelet transform is established. A filter bank is designed using a frequency-domain method due to the complex perfect reconstruction condition. Its fast implementation algorithm is investigated with the equivalent filter bank and fast Fourier transform. Compared with conventional wavelet transforms (particularly analytic flexible wavelet transform, orthogonal wavelet transform, and biorthogonal wavelet transform in this study), the proposed wavelet transform achieves better denoising performance. Lastly, a new fault diagnosis method for detecting faults in planetary gear transmission systems is developed on the basis of the proposed wavelet transform and spectral negentropy [40]. The experimental results of the planetary transmission fault diagnosis validate the superiority of the developed method over other conventional approaches, including analytic wavelet transform, Morlet wavelet transform, squared envelope (SE) infogram, and SE spectrum (SES) infogram.

2. Construction of M-band flexible wavelet transform

In this study, we focus on constructing an M-band wavelet transform with rational dilation ($M = 2$). The proposed flexible transform is realized via an analysis filter bank, and its corresponding synthesis filter bank is shown in Fig. 1. As shown in the figure, the filter bank consists of three channels, and the rational dilation factors can be tuned in accordance with the requirements of time-frequency sampling.

2.1. Perfect construction condition

To obtain a perfect reconstruction condition for the proposed wavelet transform, we first assume that all the filters, namely, $H(\omega)$, $G_1(\omega)$, and $G_2(\omega)$, are band-limited, and $q > p$, $s_1 > r_1$, and $s_2 > r_2$. In particular, suppose that filter $H(\omega)$ is supported on a single interval $[\omega_p, \omega_s]$, and the bandwidth satisfies

$$\omega_s - \omega_p \leqslant 2\pi/q \quad (1)$$

Then, the first channel in Fig. 1 exhibits the following frequency response based on multirate system theory [41]:

$$T_0(\omega) = \frac{1}{pq} \sum_{j=0}^{p-1} \left| H\left(\frac{\omega}{p} + j\frac{2\pi}{p}\right) \right|^2 \quad (2)$$

Similarly, if the bandwidths of $G_1(\omega)$ and $G_2(\omega)$ satisfy a similar condition, then we can obtain the frequency responses of the second and third channels. These responses are given by

$$T_1(\omega) = \frac{1}{r_1 s_1} \sum_{j=0}^{r_1-1} \left| G_1\left(\frac{\omega}{r_1} + j\frac{2\pi}{r_1}\right) \right|^2 \quad (3)$$

$$T_2(\omega) = \frac{1}{r_2 s_2} \sum_{j=0}^{r_2-1} \left| G_2\left(\frac{\omega}{r_2} + j\frac{2\pi}{r_2}\right) \right|^2 \quad (4)$$

From Eqs. (2)–(4), the proposed filter bank system in Fig. 1 exhibits the following frequency response:

$$T(\omega) = T_0(\omega) + T_1(\omega) + T_2(\omega) = \frac{1}{pq} \sum_{j=0}^{p-1} \left| H\left(\frac{\omega}{p} + j\frac{2\pi}{p}\right) \right|^2 + \frac{1}{r_1 s_1} \sum_{j=0}^{r_1-1} \left| G_1\left(\frac{\omega}{r_1} + j\frac{2\pi}{r_1}\right) \right|^2 + \frac{1}{r_2 s_2} \sum_{j=0}^{r_2-1} \left| G_2\left(\frac{\omega}{r_2} + j\frac{2\pi}{r_2}\right) \right|^2 \quad (5)$$

To achieve perfect reconstruction, the frequency response $T(\omega)$ must satisfy

$$T(\omega) = 1 \quad (6)$$

2.2. Filter bank design

Under a perfect reconstruction condition, designing filters in the time domain is extremely difficult, particularly when dilation factors are expected to be arbitrarily specified. Consequently, we adopt the frequency-domain filter design method used in [36]. The primary objective of the proposed transform is to increase the sampling density of a time-frequency plane. The three channels in Fig. 1 are set as low-pass, band-pass, and high-pass channels. The frequency responses of the designed filters $H(\omega)$, $G_1(\omega)$, and $G_2(\omega)$ are illustrated in Fig. 2, where α and β are the filter parameters that partly determine the passband of the three filters.

The figure shows the passbands and transition bands of the three filters. For Eqs. (2)–(4) to hold, we can easily determine from Eq. (1) that the bandwidths of the three band-limited filters should satisfy

$$\frac{\pi}{q} - 0 \leqslant \frac{2\pi}{q}, (1 - \beta) \frac{\pi}{p_1} \geqslant 0, \frac{\pi}{s_1} - (1 - \beta) \frac{\pi}{r_1} \leqslant \frac{2\pi}{s_1}, \frac{\pi}{r_2} - \frac{\alpha\pi}{r_2} \leqslant \frac{2\pi}{s_2} \quad (7)$$

From the preceding inequalities, we immediately derive

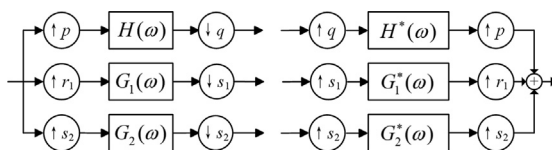


Fig. 1. Analysis and synthesis filter banks of the proposed flexible transform.

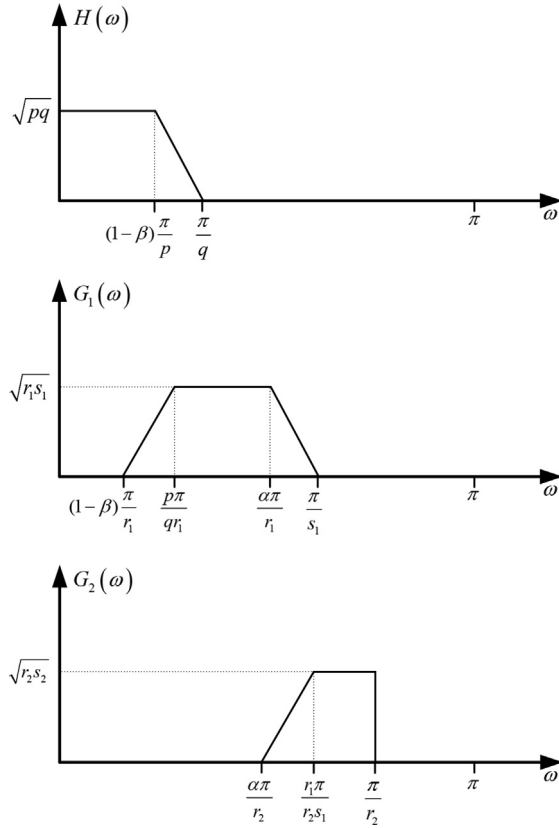


Fig. 2. Frequency responses of the filters used in the proposed wavelet transform.

$$\alpha \geq 1 - \frac{2r_2}{s_2}, \beta \leq 1 \quad (8)$$

Moreover, we easily determine from Fig. 2 that

$$\frac{\pi}{q} \geq (1-\beta)\frac{\pi}{p}, \quad \frac{p\pi}{qr_1} \geq (1-\beta)\frac{\pi}{r_1} \quad (9)$$

$$\frac{\alpha\pi}{r_1} \geq \frac{p\pi}{qr_1}, \quad \frac{\pi}{s_1} \geq \frac{\alpha\pi}{r_1}, \quad \frac{r_1\pi}{r_2s_1} \geq \frac{\alpha\pi}{r_2}, \quad \frac{\pi}{r_2} \geq \frac{r_1\pi}{r_2s_1} \quad (10)$$

From the preceding inequalities, we can derive

$$\beta \geq 1 - \frac{p}{q} \quad (11)$$

$$\alpha \geq \frac{p}{q}, \quad \alpha \leq \frac{r_1}{s_1} \quad (12)$$

Following Eqs. (8), (11), and (12), we obtain

$$\max\left(\frac{p}{q}, 1 - \frac{2r_2}{s_2}\right) \leq \alpha \leq \frac{r_1}{s_1} \quad (13)$$

$$1 - \frac{p}{q} \leq \beta \leq 1 \quad (14)$$

To satisfy the perfect reconstruction condition, the filter bank can be designed via the following proposition on the basis of the frequency responses of the three filters illustrated in Fig. 2.

Proposition 1. Let $\theta(\omega)$ be a function that satisfies

$$|\theta(\omega)|^2 + |\theta(\pi - \omega)|^2 = 1, \omega \in [0, \pi] \quad (15)$$

Let α and β be constrained by Eqs. (13) and (14), respectively. Suppose that the frequency responses of the filters $H(\omega)$, $G_1(\omega)$, and $G_2(\omega)$ are defined as

$$H(\omega) = \begin{cases} \sqrt{pq}\theta\left(\frac{\omega + \omega_p}{\omega_s - \omega_p}\pi\right) & -\omega_s \leq \omega \leq -\omega_p \\ \sqrt{pq} & |\omega| < \omega_p \\ \sqrt{pq}\theta\left(\frac{\omega - \omega_p}{\omega_s - \omega_p}\pi\right) & \omega_p \leq \omega \leq \omega_s \\ 0 & |\omega| > \omega_s \end{cases} \quad (16)$$

$$G_1(\omega) = \begin{cases} \sqrt{r_1 s_1}\theta\left(\frac{\omega + \omega_2}{\omega_3 - \omega_2}\pi\right) & -\omega_3 < \omega < -\omega_2 \\ \sqrt{r_1 s_1}\theta\left(\pi + \frac{\omega + \omega_0}{\omega_1 - \omega_0}\pi\right) & -\omega_1 < \omega < -\omega_0 \\ \sqrt{r_1 s_1} & \omega_1 \leq |\omega| \leq \omega_2 \\ \sqrt{r_1 s_1}\theta\left(\pi - \frac{\omega - \omega_0}{\omega_1 - \omega_0}\pi\right) & \omega_0 < \omega < \omega_1 \\ \sqrt{r_1 s_1}\theta\left(\frac{\omega - \omega_2}{\omega_3 - \omega_2}\pi\right) & \omega_2 < \omega \leq \omega_3 \\ 0 & |\omega| > \omega_3 \text{ or } |\omega| < \omega_0 \end{cases} \quad (17)$$

$$G_2(\omega) = \begin{cases} \sqrt{r_2 s_2}\theta\left(\pi + \frac{\omega + \omega_4}{\omega_5 - \omega_4}\pi\right) & -\omega_5 < \omega < -\omega_4 \\ \sqrt{r_2 s_2} & \omega_5 \leq |\omega| \leq \omega_6 \\ \sqrt{r_2 s_2}\theta\left(\pi - \frac{\omega - \omega_4}{\omega_5 - \omega_4}\pi\right) & \omega_4 < \omega < \omega_5 \\ 0 & |\omega| > \omega_6 \end{cases} \quad (18)$$

where $\omega_p = (1 - \beta)\pi/p$, $\omega_s = \pi/q$, $\omega_0 = (1 - \beta)\pi/r_1$, $\omega_1 = p\pi/(qr_1)$, $\omega_2 = \alpha\pi/r_1$, $\omega_3 = \pi/s_1$, $\omega_4 = \alpha\pi/r_2$, $\omega_5 = r_1\pi/(r_2s_1)$, and $\omega_6 = \pi/r_2$. The analysis and synthesis filter banks exhibit perfect reconstruction property.

Proof. When Eqs. (16)–(18) are substituted into Eq. (5), Eq. (6) holds. Therefore, Proposition 1 is proven.

A typical function $\theta(\omega)$ can be adopted similar to that in [36,38,42].

$$\theta(\omega) = \frac{1}{2}(1 + \cos\omega)\sqrt{2 - \cos\omega} \quad (19)$$

This transition function satisfies Eq. (15). The design of the filter bank is completed using Eqs. (16)–(19). From the designed filter bank, we determine that the proposed transform samples the time–frequency plane as illustrated in Fig. 3. Evidently, the sampling rate of the second channel at the i th stage is $(p/q)^{i-1}(r_1/s_1)$, and the sampling rate of the third channel at the i th stage is $(p/q)^{i-1}(r_2/s_2)$. The redundancy of the proposed transform is given by

$$R = (r_1/s_1) \sum_{i=1}^{\infty} \left(\frac{p}{q}\right)^{i-1} + (r_2/s_2) \sum_{i=1}^{\infty} \left(\frac{p}{q}\right)^{i-1} = (r_1/s_1 + r_2/s_2) \frac{1}{1 - p/q} \quad (20)$$

3. Numerical implementation

The proposed M-band flexible wavelet transform is implemented by the iterative filter banks shown in Fig. 4. Assume that c_1^i denotes the wavelet coefficients of the second channel at the i th stage and c_2^i denotes the wavelet coefficients of the third channel at the i th stage. In accordance with Eqs. (17) and (18), the frequency supports of c_1^i and c_2^i in the first stage are defined as

$$F(c_1^1) = \left[(1 - \beta)\pi, \frac{r_1\pi}{s_1}\right] \quad (21)$$

$$F(c_2^1) = [\alpha\pi, \pi] \quad (22)$$

From Eq. (16), the frequency support of $H(\omega)$ is $[-\pi/q, \pi/q]$. Thus, the frequency supports of c_1^2 and c_2^2 in the second stage are defined as

$$F(c_1^2) = \left[\frac{p}{q}(1 - \beta)\pi, \frac{p}{q}\frac{r_1\pi}{s_1}\right] \quad (23)$$

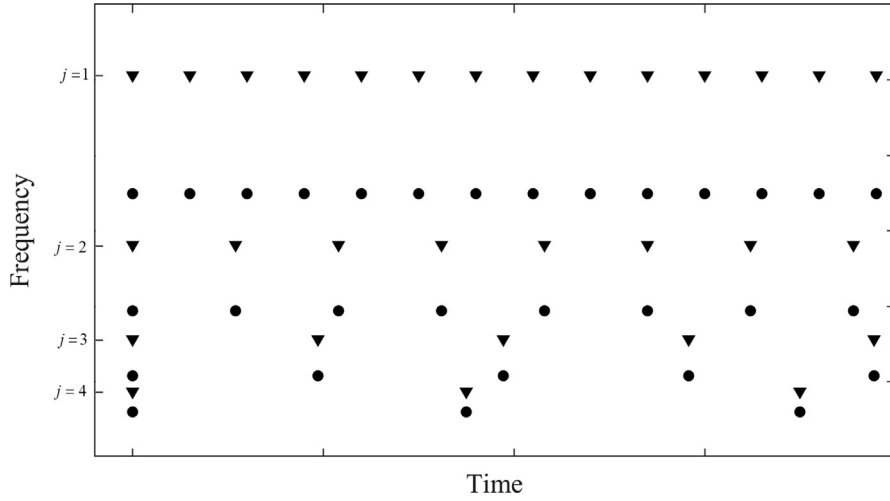


Fig. 3. Time–frequency sampling of the proposed wavelet transform.

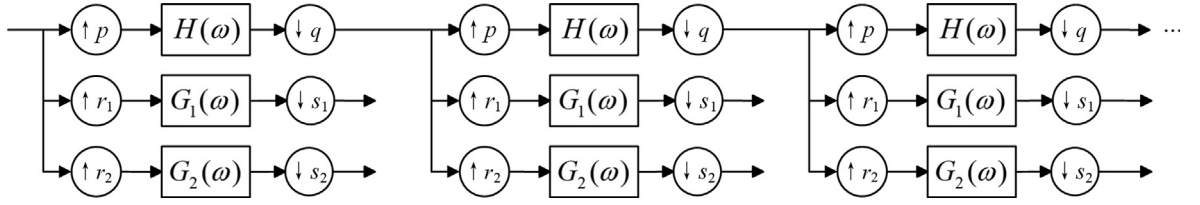


Fig. 4. Iterative filter banks of the proposed wavelet transform.

$$F(c_2^2) = \left[\frac{p}{q} \alpha \pi, \frac{p}{q} \pi \right] \quad (24)$$

Through an induction argument, the frequency supports of c_1^i and c_2^i can be derived as

$$F(c_1^i) = \left[\left(\frac{p}{q} \right)^{i-1} (1 - \beta) \pi, \left(\frac{p}{q} \right)^{i-1} \frac{r_1 \pi}{s_1} \right] \quad (25)$$

$$F(c_2^i) = \left[\left(\frac{p}{q} \right)^{i-1} \alpha \pi, \left(\frac{p}{q} \right)^{i-1} \pi \right] \quad (26)$$

On the basis of multirate filter bank theory, Fig. 4 can be equivalent to Fig. 5. Given that $q_1 = N$, $s_{1,1} = N/2$, and $s_{2,1} = N/2$, the sampling parameters in Fig. 5 are defined as

$$p_i = 2 \left\lfloor \frac{p^i}{2q^i} N \right\rfloor \quad q_{i+1} = p_i \quad (27)$$

$$r_{1,i} = \left\lfloor \frac{r_1}{s_1} \frac{p^{i-1}}{q^{i-1}} N \right\rfloor \quad s_{1,i+1} = p_i/2 \quad (28)$$

$$r_{2,i} = \left\lfloor \frac{r_2}{s_2} \frac{p^{i-1}}{q^{i-1}} N \right\rfloor \quad s_{2,i+1} = p_i/2 \quad (29)$$

Assume that

$$H^{(1)}(\omega) = H(\omega) \quad G_1^{(1)}(\omega) = G_1(\omega) \quad G_2^{(1)}(\omega) = G_2(\omega) \quad (30)$$

In accordance with the frequency supports of the wavelet coefficients, we can obtain the following from Figs. 2 and 5:

$$H^{(n)}(\omega) = \begin{cases} \frac{1}{p_{n-1}} H^{(n-1)}\left(\frac{p_n}{p_{n-1}} \omega\right) H\left(\frac{q_1}{p_{n-1}} \omega\right) & |\omega| \leq \pi/q_1 \\ 0 & \pi/q_1 < |\omega| \leq \pi \end{cases} \quad (31)$$

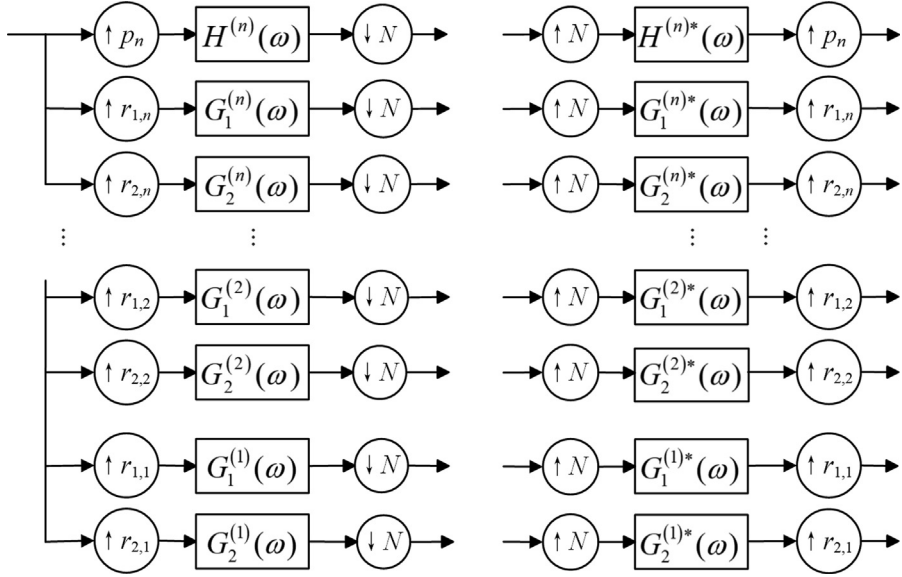


Fig. 5. Equivalent filter banks of the proposed wavelet transform.

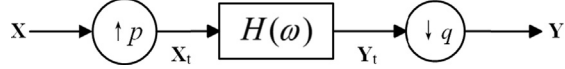


Fig. 6. Typical rational rate changer.

$$G_1^{(n)}(\omega) = \begin{cases} 0 & 0 \leq |\omega| < \frac{p_{n-1}(1-\beta)}{q_1 r_{1,n}} \\ \frac{1}{p_{n-1}} H^{(n-1)}\left(\frac{r_{1,n}}{p_{n-1}}\omega\right) G_1\left(\frac{q_1}{p_{n-1}}\omega\right) & \frac{p_{n-1}(1-\beta)}{q_1 r_{1,n}} \pi \leq |\omega| \leq \frac{p_{n-1}}{q_1 s_{1,n}} \pi \\ 0 & \frac{p_{n-1}}{q_1 s_{1,n}} \pi < |\omega| \leq \frac{\pi}{q_1} \end{cases} \quad (32)$$

$$G_2^{(n)}(\omega) = \begin{cases} 0 & 0 \leq |\omega| < \frac{p_{n-1}\alpha}{q_1 r_{2,n}} \pi \\ \frac{1}{p_{n-1}} H^{(n-1)}\left(\frac{r_{2,n}}{p_{n-1}}\omega\right) G_2\left(\frac{q_1}{p_{n-1}}\omega\right) & \frac{p_{n-1}\alpha}{q_1 r_{2,n}} \pi \leq |\omega| \leq \frac{p_{n-1}}{q_1 r_{2,n}} \pi \\ 0 & \frac{p_{n-1}}{q_1 r_{2,n}} \pi < |\omega| \leq \frac{\pi}{q_1} \end{cases} \quad (33)$$

Notably, the filter banks are composed of a series of rational rate changers. A typical rational rate changer is shown in Fig. 6. For a discrete time signal, this changer can be implemented via discrete Fourier transform (DFT). The DFT of a time series \mathbf{x} with N -length is defined as

$$X(k) = \frac{1}{\sqrt{N}} \sum_{n=0}^{N-1} x(n) e^{-j \frac{2\pi}{N} nk}, \quad 0 \leq k \leq N-1 \quad (34)$$

Consider a specific example to explain the numerical implementation of this rate changer. Assume that $p = 2$, $q = 3$, and $N = 6$. The length of \mathbf{Y} is calculated as $Np/q = 4$. Fig. 6 shows that \mathbf{X}_t is the DFT of the upsampled signal, and it can be obtained by repeating \mathbf{X} twice in sequence. Let \mathbf{H} denote the corresponding discrete sequence of $H(\omega)$, and we derive $\mathbf{Y}_t = \mathbf{X}_t \mathbf{H}$. By using three blocks, namely, \mathbf{Y}_1 , \mathbf{Y}_2 , and \mathbf{Y}_3 , we can compute \mathbf{Y} with

$$Y(k) = \frac{1}{4} \sum_{n=0}^3 Y_u(k + 4n), \quad k = 0, 1, 2, 3 \quad (35)$$

To hasten computation, we use another implementation method based on shift, which is found in [38].

4. Simulation and comparison

By using the numerical implementation algorithm of the proposed flexible transform and the cascade algorithm [43], we can construct the corresponding wavelets with the given filter parameters $p, q, r_1, s_1, r_2, s_2, \alpha$, and β . The constructed wavelets

must satisfy Eqs. (21) and (22). For simplification, parameters r_1 and s_1 can be set as $r_1 = r_2$ and $s_1 = s_2$, respectively, in most cases. Two examples are provided to demonstrate how sampling density and filter parameters determine the properties of the designed wavelets, such as wavelet support, oscillation frequency, translation, and dilation factor.

- 1) Example 1: We set $(p, q, r_1, s_1, r_2, s_2, \alpha, \beta) = (2, 3, 7, 9, 7, 9, \frac{13}{18}, \frac{8}{9})$. With respect to the two filters $G_1(\omega)$ and $G_2(\omega)$, the two corresponding wavelets are illustrated in Fig. 7.
- 2) Example 2: In contrast with Example 1, the sampling factors of the second and third channels are different in this example. The filter parameters are set as $(p, q, r_1, s_1, r_2, s_2, \alpha, \beta) = (1, 2, 3, 4, 5, 7, \frac{9}{16}, \frac{5}{8})$, and the two corresponding wavelets are illustrated in Fig. 8.

From the comparison of Figs. 7 and 8, we can determine from Eqs. (25) and (26) that the second wavelet ψ_2 in Example 1 has a longer support and higher oscillation frequency than that in Example 2 due to the smaller α (i.e., the third filter channel in Example 2 has a wider frequency band). Meanwhile, the first wavelet ψ_1 in Example 1 has a shorter support than that in Example 2 due to the larger β and r_1/s_1 (i.e., the second filter channel in Example 1 has a wider frequency band). Evidently, different wavelet shapes can be obtained by changing the value of each parameter. Therefore, we can select appropriate parameters to construct M-band flexible wavelets in accordance with the characteristics of the analyzed signal. Moreover, by maximizing several measurement indices, such as kurtosis, entropy, and the correlation coefficient, the optimized wavelets can be found by several optimization algorithms (e.g., particle swarm algorithm and genetic algorithm). This phenomenon will be explored in the future.

To demonstrate the superiority of the proposed flexible wavelet transform, denoising experiments were performed. The analytic wavelet transform in [38], orthogonal wavelet transform, and biorthogonal wavelet transform were used for comparison. For the proposed transform, we set $(p, q, r_1, s_1, r_2, s_2, \alpha, \beta) = (2, 3, 7, 9, 7, 9, \frac{13}{18}, \frac{8}{9})$. For the analytic wavelet transform, we similarly set $(p, q, r, s, \beta) = (2, 3, 7, 9, \frac{8}{9})$ in accordance with the parameters of the proposed transform. For the orthogonal wavelet transform, the Daubechies wavelets with two vanishing moments were used. For the biorthogonal wavelet transform, the biorthogonal wavelets “bior3.9” were used. A “piece-regular” signal with 4096 points generated via the WaveLab software package was used as the original test signal. We first normalized the signal and then added an independent white zero-mean Gaussian random noise with a standard derivation of 0.28. The root-mean-square (RMS) error between the denoised signal and the noisy signal was calculated as a function of the threshold value. For each wavelet transform, we performed six stages of decomposition and reconstruction. When the threshold value ranged from 0.4 to 1.1, the results obtained from averaging 100 realizations are shown in Fig. 9. The proposed wavelet transform achieves the best denoising performance, whereas biorthogonal wavelet transform exhibits the worst denoising performance, particularly when the threshold is small, because the proposed transform has the highest time-frequency sampling density. Notably, the denoising performance of analytic wavelet transform increasingly approximated that of the proposed M-band flexible wavelet

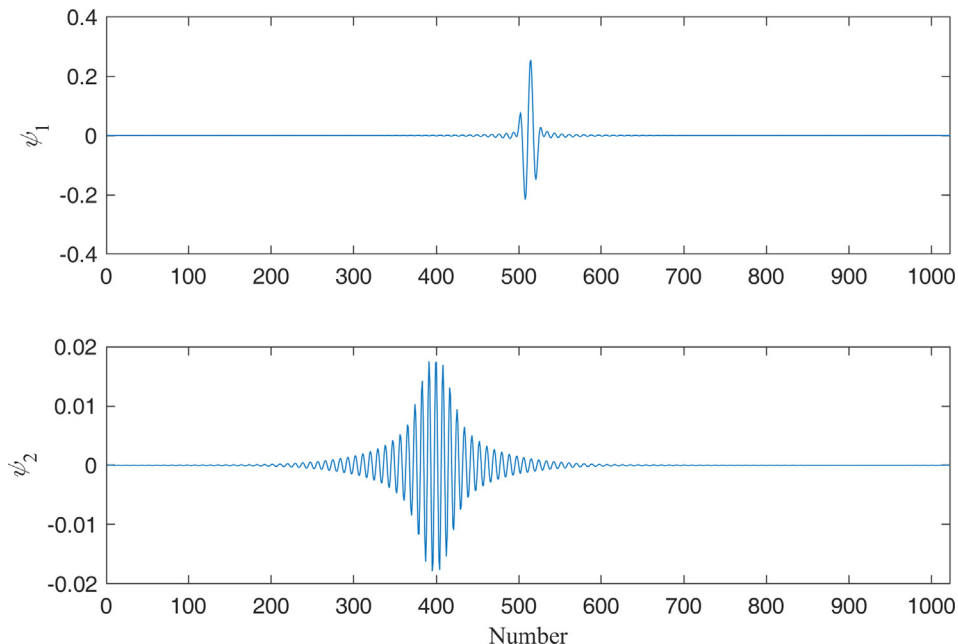


Fig. 7. Time-domain waveforms of two wavelets (ψ_1 and ψ_2) in Example 1.

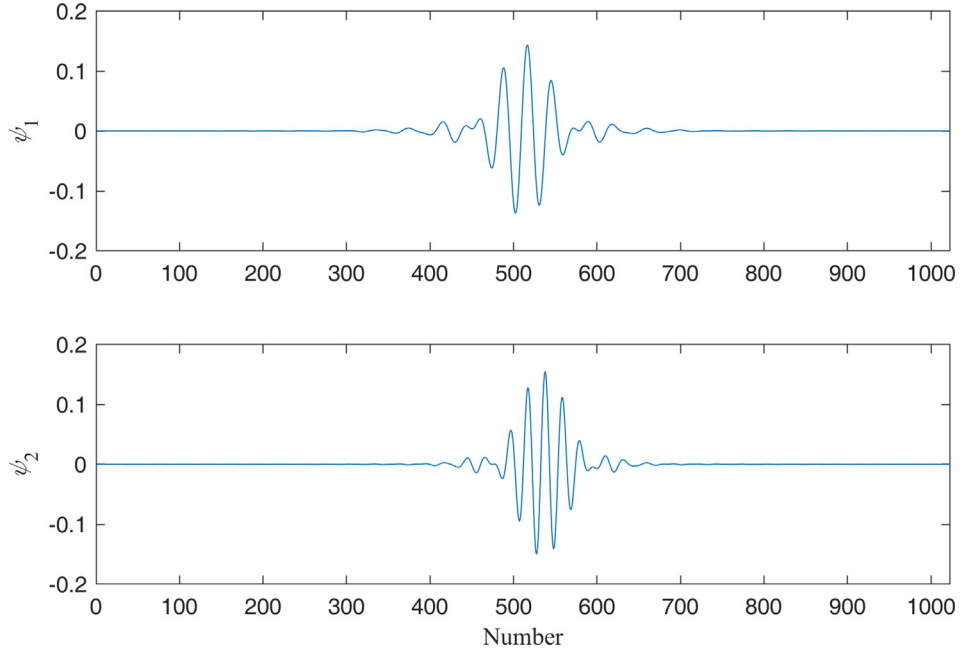


Fig. 8. Time-domain waveforms of two wavelets (ψ_1 and ψ_2) in Example 2.

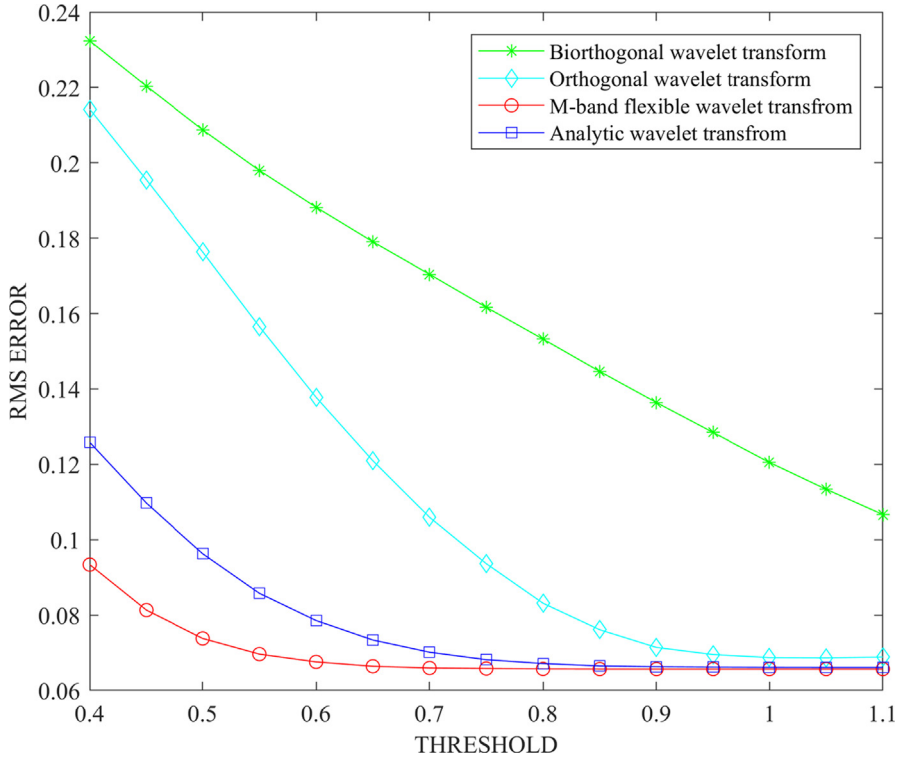


Fig. 9. Comparison of denoising performance for a noisy ‘piece-regular’ signal.

transform with an increase in threshold. The smaller the threshold, the better impulsive feature is extracted. Therefore, the proposed M-band flexible wavelet transform is highly suitable for processing the vibration signals of planetary gear transmission systems with gear damages.

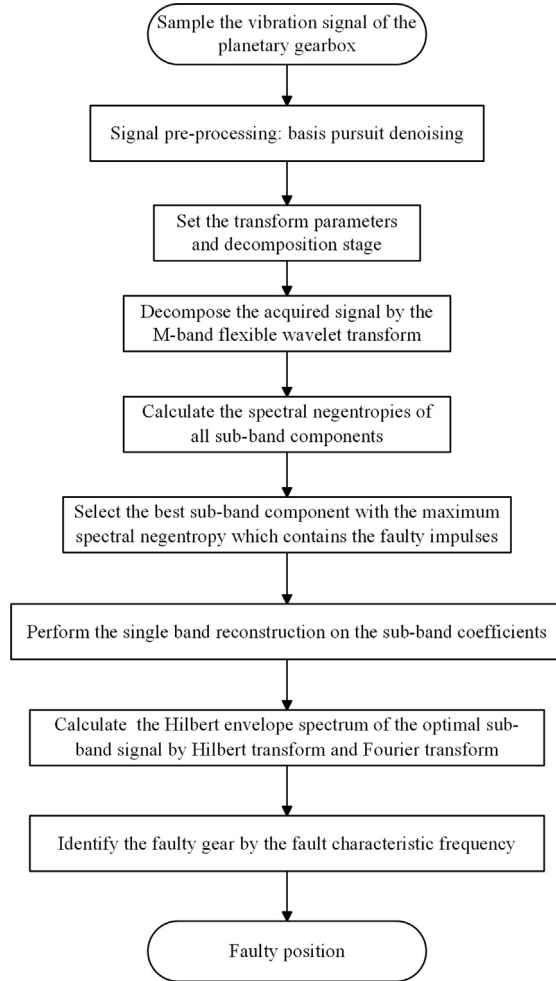


Fig. 10. Flowchart of the proposed fault diagnosis method for planetary transmission systems.

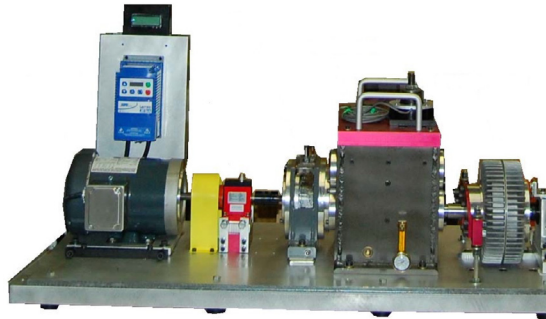


Fig. 11. Test rig for planetary transmission fault diagnosis.

5. Application to planetary transmission fault diagnosis

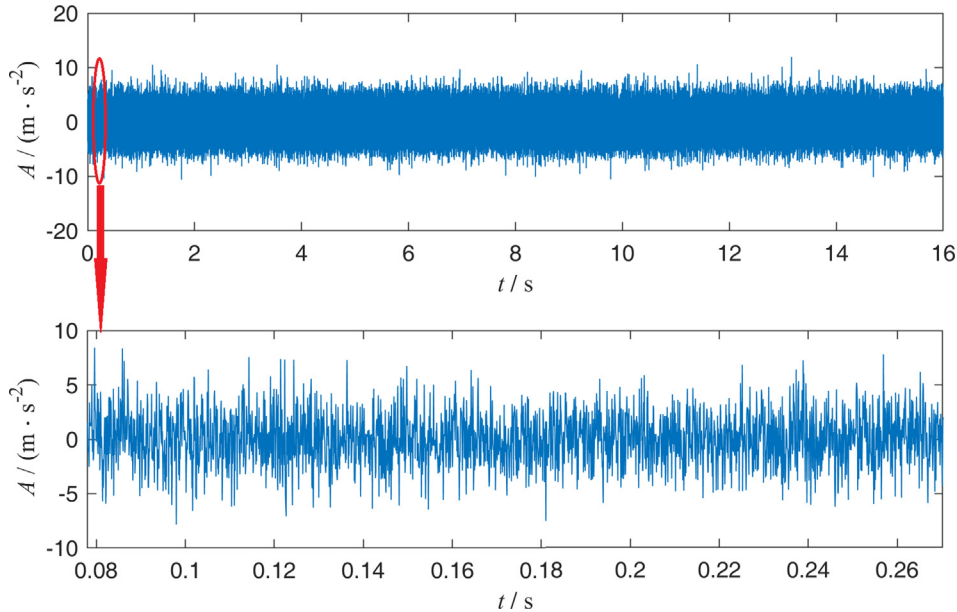
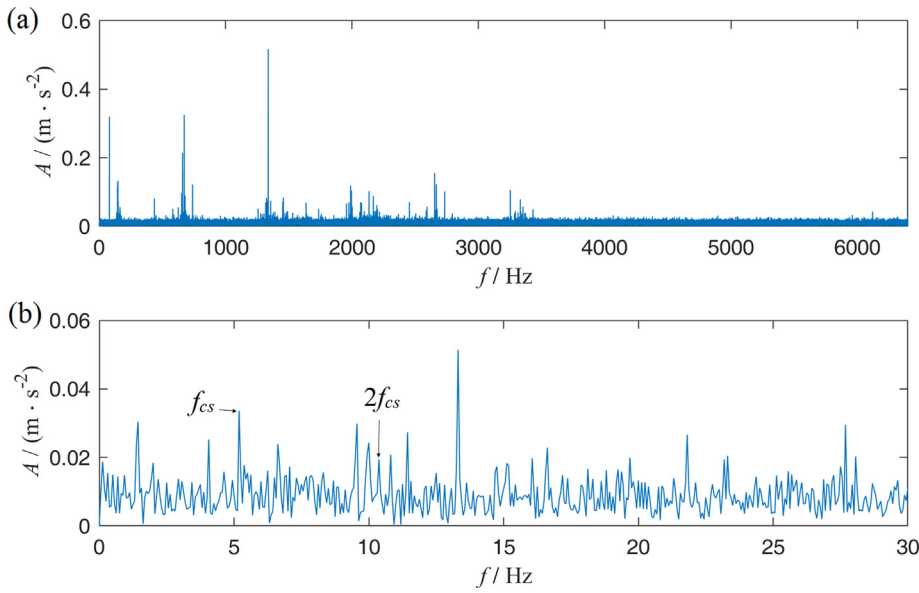
5.1. Fault diagnosis method

When the gear of a planetary transmission system suffers a damage, periodic impulses will be produced. The fault of the gear can be diagnosed by detecting the cyclic frequency of repetitive impulses. For early faults, however, a periodically impulsive characteristic is frequently submerged in noise and other vibration components. Kurtosis is an efficient and pop-

Table 1

Configuration parameters of the two-stage planetary gearbox.

Level	Tooth number of sun gear	Tooth number of planet gear	Tooth number of ring gear	Number of planet gears
First stage	20	40	100	3
Second stage	28	36	100	4

**Fig. 12.** Time-domain waveform of a planetary gearbox vibration signal with micropitting fault and a segment between 0.078 s and 0.2763 s.**Fig. 13.** Frequency-domain analysis of a planetary gearbox vibration signal with micropitting fault: (a) frequency spectrum and (b) envelope spectrum.

ular index for detecting impulses (transients); meanwhile, recent research shows that spectral negentropy exhibits better ability to identify weak transients [40]. Consequently, a new planetary transmission fault diagnosis method based on M-band flexible wavelet transform and spectral negentropy is proposed to detect weak faulty features. First, the acquired vibration signal of a planetary gearbox is preprocessed via basis pursuit denoising to remove random noise. Second, the

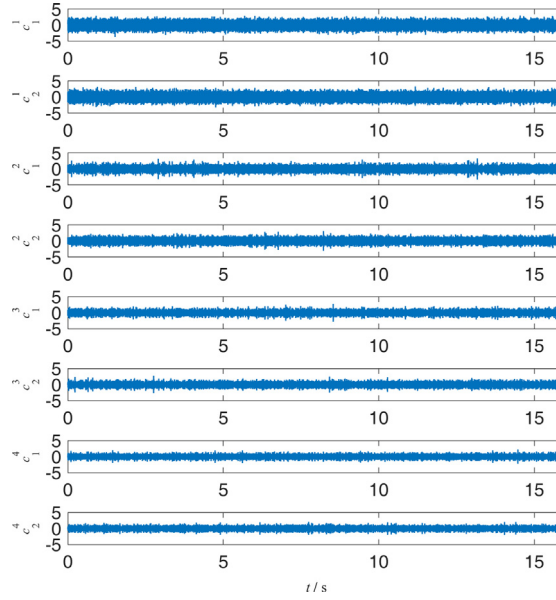


Fig. 14. Obtained wavelet coefficients of a planetary gearbox vibration signal with micropitting fault.

preprocessed signal is decomposed via M-band flexible wavelet transform. Third, the best sub-band that contains distinct transients caused by the fault is selected via spectral negentropy, which is defined as

$$H_e(f; \Delta f) = \left\langle \frac{\varepsilon_x(n; f, \Delta f)^2}{\langle \varepsilon_x(n; f, \Delta f)^2 \rangle} \ln \left(\frac{\varepsilon_x(n; f, \Delta f)^2}{\langle \varepsilon_x(n; f, \Delta f)^2 \rangle} \right) \right\rangle \quad (36)$$

where

$$\varepsilon_x(n; f, \Delta f) = |x(n; f, \Delta f)|^2 \quad (37)$$

and $x(n; f, \Delta f)$ denotes the complex envelope of a discrete time signal $x(n)$ within the frequency range of $[f - \Delta f/2; f + \Delta f/2]$. This frequency range is used to calculate spectral negentropy through Eq. (36). Fourth, single band reconstruction is performed on the sub-band coefficients to obtain the sub-band signal with the same length as the original signal. Fifth, the Hilbert envelope spectrum of the optimal sub-band signal is calculated to obtain the fault characteristic frequency. Lastly, the damaged gear can be localized on the basis of fault characteristic frequency. The flowchart of the proposed fault diagnosis method is provided in Fig. 10.

5.2. Fault diagnosis of gear micropitting

Micropitting is an early gear fault, and detecting such fault is beneficial to prevent a serious catastrophe. However, when the tooth surface of a planetary gearbox's gear generates micropitting, the fault feature is extremely weak, and accurately recognizing this fault is difficult using traditional methods. Therefore, the proposed fault diagnosis method was applied

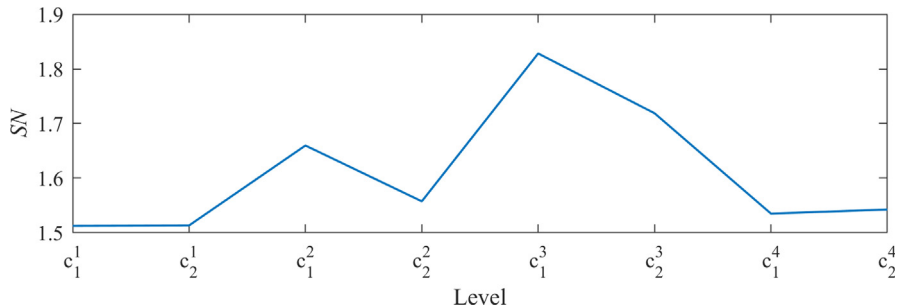


Fig. 15. Spectral negentropies of the wavelet coefficients of a planetary gearbox vibration signal with micropitting fault.

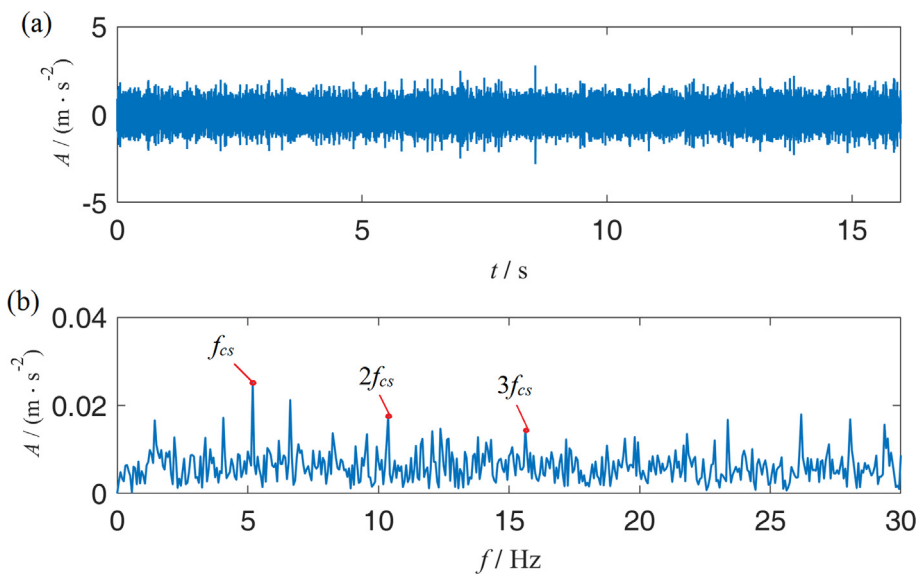


Fig. 16. Detection result of a planetary gearbox vibration signal with micropitting fault obtained using the proposed method: (a) time-domain waveform and (b) envelope spectrum.



Fig. 17. Tooth surfaces of the sun gear with micropitting fault.

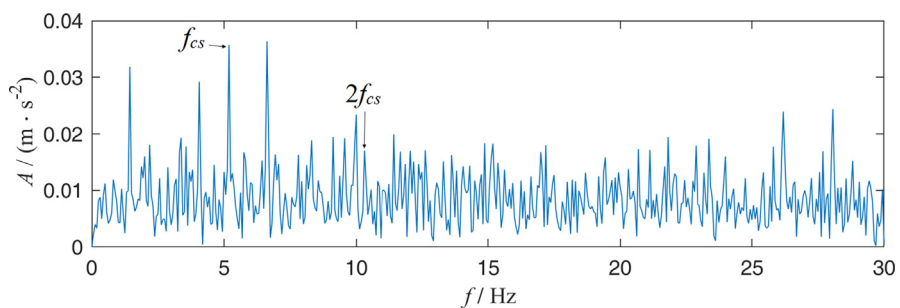


Fig. 18. Envelope spectrum for the sun gear micropitting fault obtained via analytic wavelet transform.

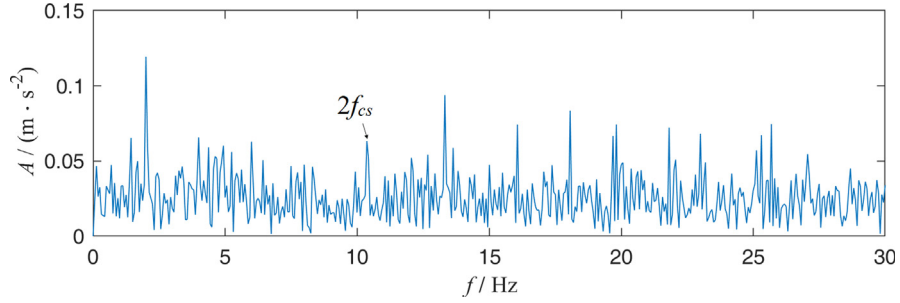


Fig. 19. Envelope spectrum for the sun gear micropitting fault obtained via Morlet wavelet transform.

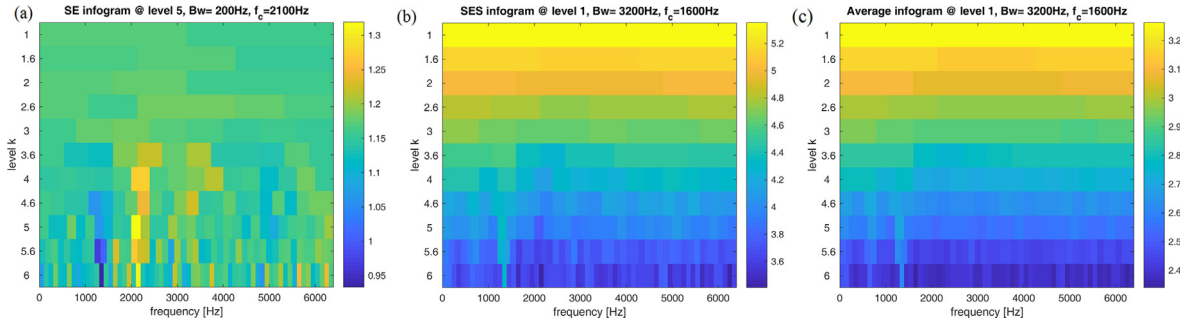


Fig. 20. Various infograms of a planetary gearbox vibration signal with micropitting fault: (a) SE infogram, (b) SES infogram, and (c) average infogram.

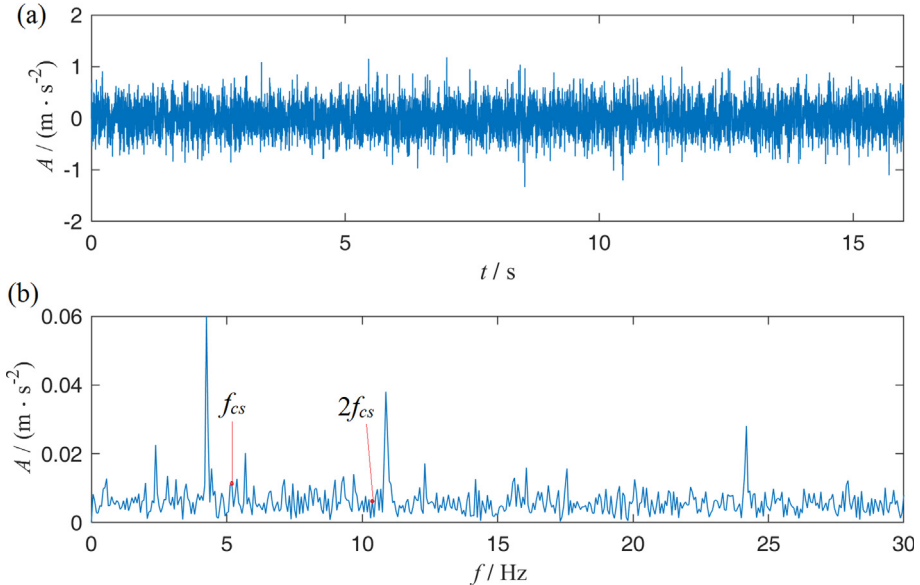


Fig. 21. Detection result of a planetary gearbox vibration signal with micropitting fault obtained using the SE infogram method: (a) time-domain waveform and (b) envelope spectrum.

to diagnose gear micropitting. A drivetrain diagnostics simulator (DDS; SpectraQuest Inc.) was used in the micropitting recognition experiment. As shown in Fig. 11, the test rig consisted of a two-stage planetary gearbox and a two-stage parallel gearbox. The configuration parameters of the two-stage planetary gearbox are listed in Table 1. In the experiment, the sun gear in the second stage had a micropitting fault, which was obtained using a gear fatigue testing machine. The input rotational speed was set as 2440 rpm. The distributed fault characteristic frequency f_{cs} was calculated as 5.2 Hz in accordance with the parameters of the experimental planetary gearbox.

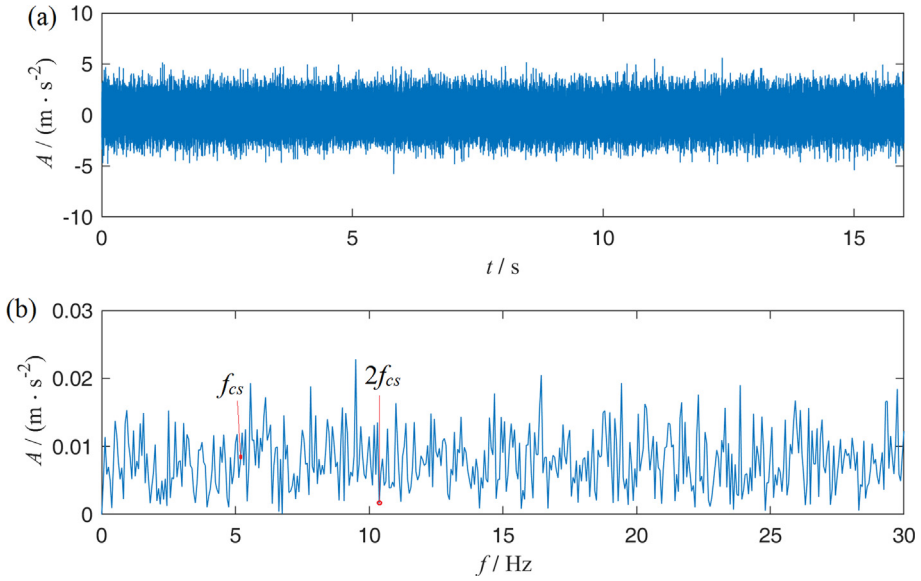


Fig. 22. Detection result of a planetary gearbox vibration signal with micropitting fault obtained using the SES infogram method: (a) time-domain waveform and (b) envelope spectrum.

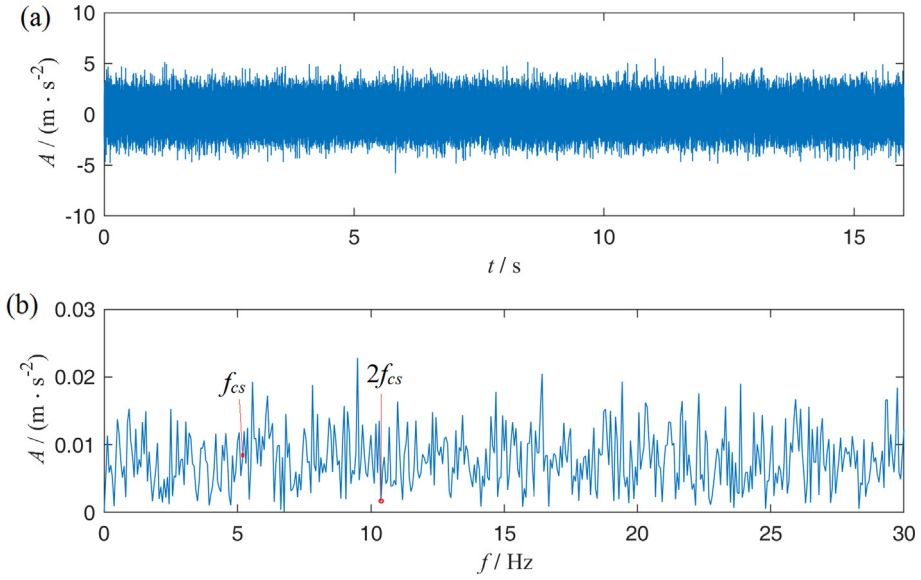


Fig. 23. Detection result of a planetary gearbox vibration signal with micropitting fault obtained using the average infogram method: (a) time-domain waveform and (b) envelope spectrum.

An accelerometer was placed on the case of the planetary gearbox to acquire the vibration signal, and the vibration signal was sampled at 12800 Hz. Its time-domain waveform and a segment between 0.078 s and 0.2763 s are illustrated in Fig. 12. The frequency spectrum and envelope spectrum of the acquired signal were computed using fast Fourier transform and Hilbert transform and illustrated in Fig. 13(a) and (b), respectively. Fig. 13(b) shows two spectral peaks with a relatively small amplitude at f_{cs} and $2f_{cs}$. Hence, the proposed wavelets in Example 1 were used to decompose this vibration signal. Through four-stage decomposition, the obtained wavelet coefficients are illustrated in Fig. 14, and their spectral negentropies were calculated as illustrated in Fig. 15. The best sub-band signal corresponds to the wavelet coefficient c_1^3 of the second channel in the third stage, as shown in Fig. 16(a). The envelope spectrum of this sub-band signal was calculated and illustrated in Fig. 16(b). Three clear spectral peaks occur at f_{cs} , $2f_{cs}$, and $3f_{cs}$, and the spectral line at f_{cs} has the largest amplitude. The sun gear in the second stage has a fault. On-site inspection indicated that the tooth surfaces of the sun gear have several micropittings, as shown in Fig. 17.

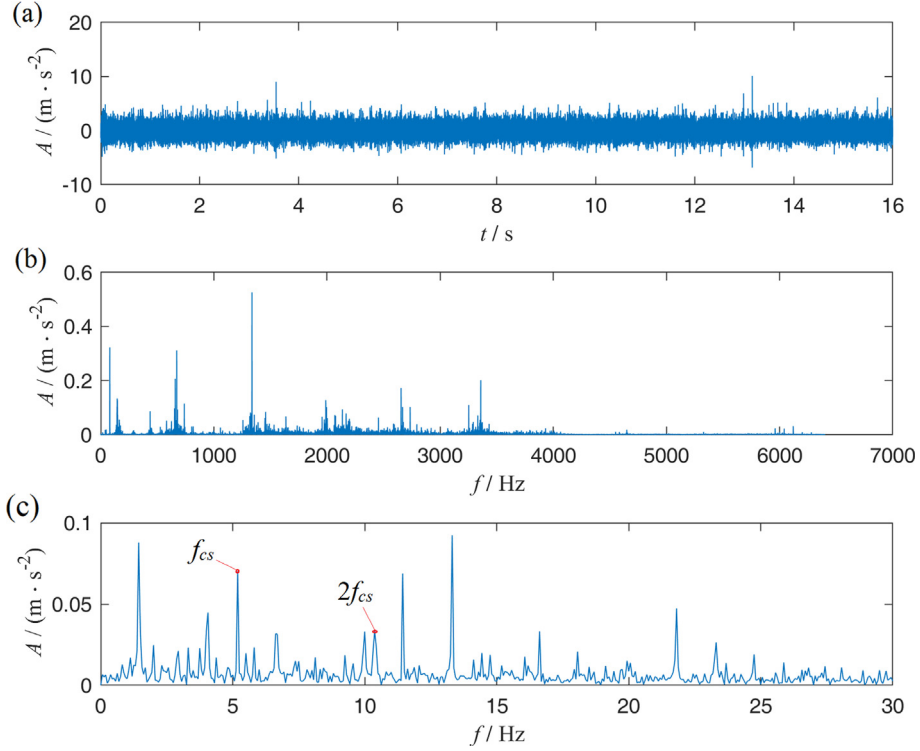


Fig. 24. Time-domain waveform and spectra of a planetary gearbox vibration signal with broken tooth fault: (a) time-domain waveform, (b) frequency spectrum, and (c) envelope spectrum.

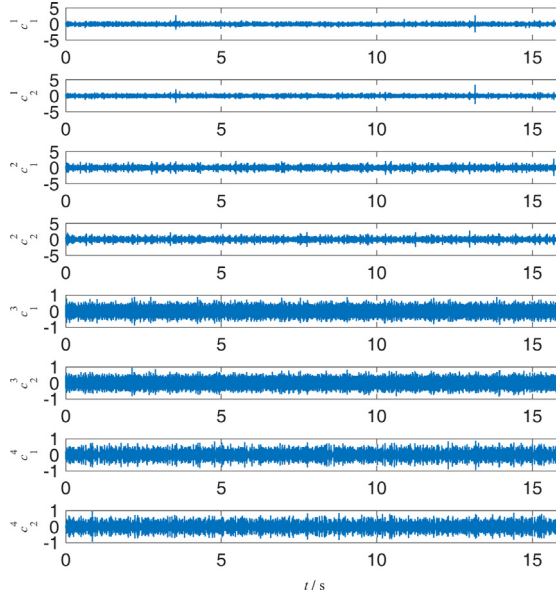


Fig. 25. Obtained wavelet coefficients of a planetary gearbox vibration signal with broken tooth fault.

Given the similarity between impulse and wavelet, several types of wavelets, such as Morlet, Laplace, and model-based impulsive wavelets [44], have been successfully applied to detect the transient feature. Among them, Morlet wavelets are the most commonly used. Thus, for the fault diagnosis process illustrated in Fig. 10, we replaced the proposed M-band flexible wavelet transform with analytic wavelet transform and Morlet wavelet transform. The fault diagnosis methods based on analytic wavelet transform and optimized Morlet wavelet transform were used for comparison. The envelope spectra of

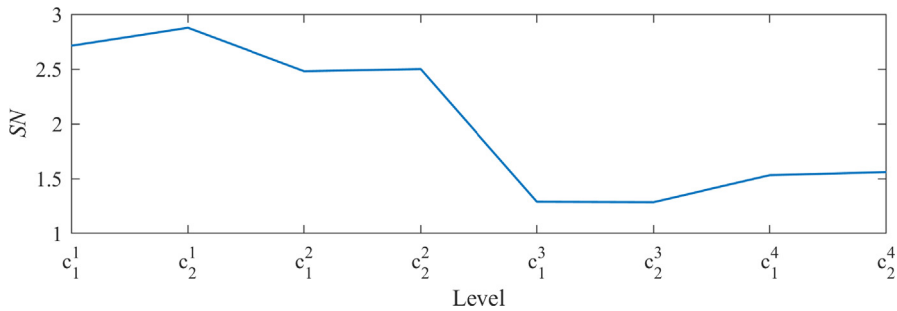


Fig. 26. Spectral negentropies of the wavelet coefficients of a planetary gearbox vibration signal with broken tooth fault.

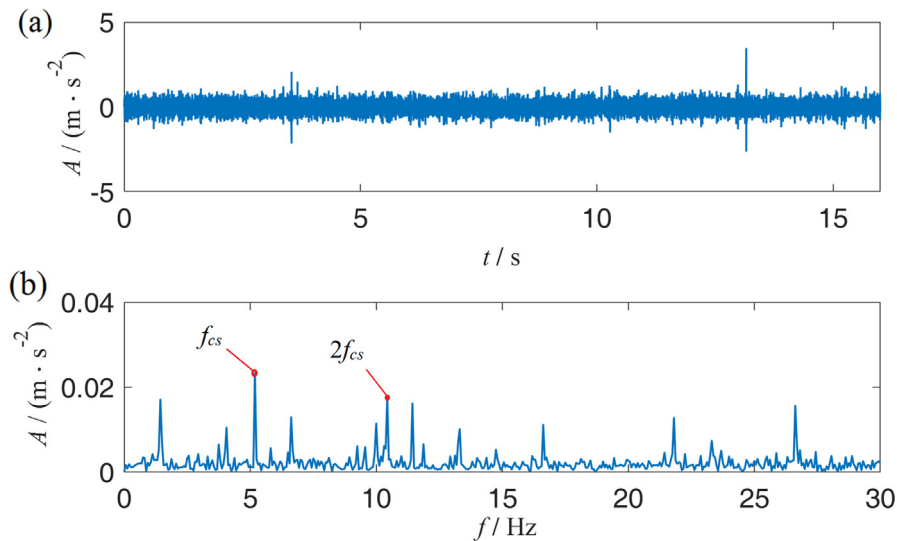


Fig. 27. Detection result of a planetary gearbox vibration signal with broken tooth fault obtained using the proposed method: (a) time-domain waveform and (b) envelope spectrum.

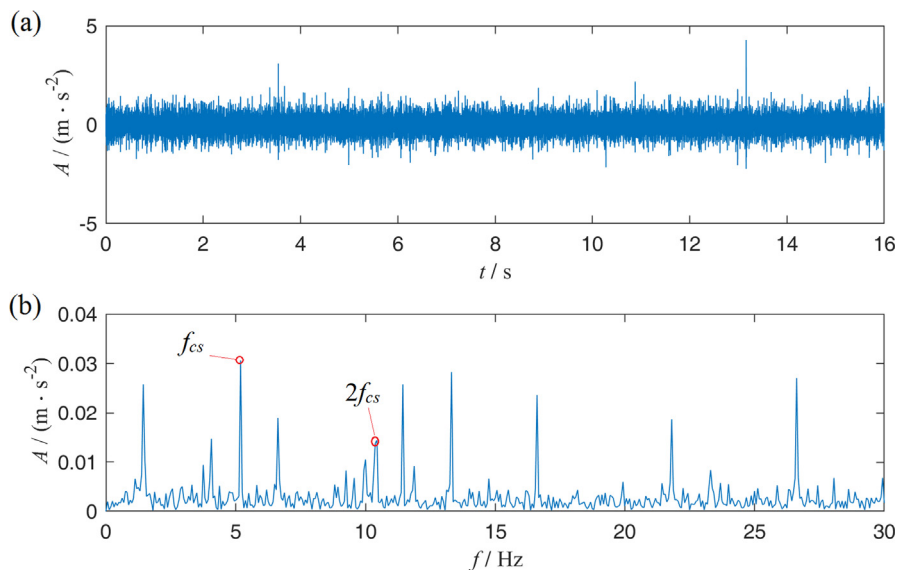


Fig. 28. Detection result of a planetary gearbox vibration signal with broken tooth fault obtained using analytic wavelet transform: (a) time-domain waveform and (b) envelope spectrum.

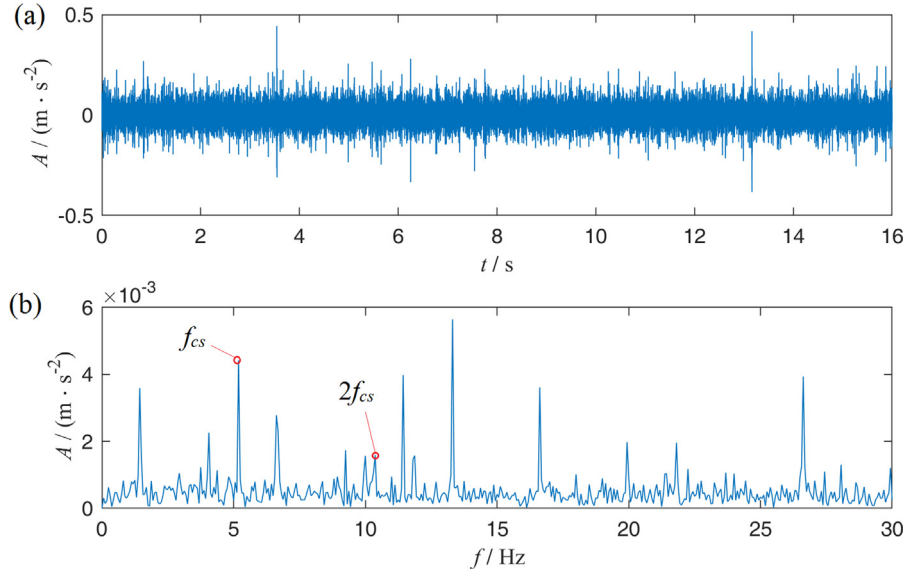


Fig. 29. Detection result of a planetary gearbox vibration signal with broken tooth fault obtained using Morlet wavelet transform: (a) time-domain waveform and (b) envelope spectrum.

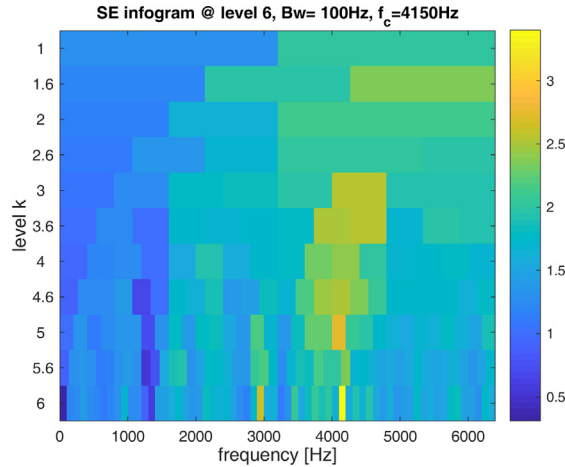


Fig. 30. SE infogram of a planetary gearbox vibration signal with broken tooth fault.

the optimal sub-band component obtained via analytic wavelet transform and optimized Morlet wavelet transform are illustrated in Figs. 18 and 19, respectively. Fig. 18 shows an apparent spectral peak at f_{cs} and a slight spectral peak at $2f_{cs}$; the spectral line at f_{cs} does not have the largest amplitude. Fig. 19 shows a slight spectral peak at $2f_c$. Thus, the proposed transform is superior to analytic wavelet transform and Morlet wavelet transform in fault feature extraction. Moreover, three infogram methods based on a filter bank, i.e., SE infogram, SES infogram, and average infogram ($\Delta I_{1/2}$), were applied to process the same vibration signal. The obtained infograms are illustrated in Fig. 20. The characteristic components were extracted using the optimal filter parameters shown in Fig. 20, and their envelope spectra were calculated. The time-domain waveform and envelope spectrum obtained using the SE infogram are shown in Fig. 21. The time-domain waveform and envelope spectrum obtained using the SES infogram are shown in Fig. 22. The SES infogram method has the same optimal filter parameters with the average infogram method, and thus, the time-domain waveform and envelope spectrum obtained using the average infogram shown in Fig. 23 are the same as those obtained in Fig. 22. In Figs. 21–23, no apparent spectral peak is observed at the fault characteristic frequency and its multiplication. From the preceding comparison, the proposed fault diagnosis method is more suitable for detecting the micropitting fault of a planetary gearbox because the filter bank used in the infogram method does not have a transition band, and the corresponding basis functions are less similar to the transients caused by the fault compared with the proposed wavelets.

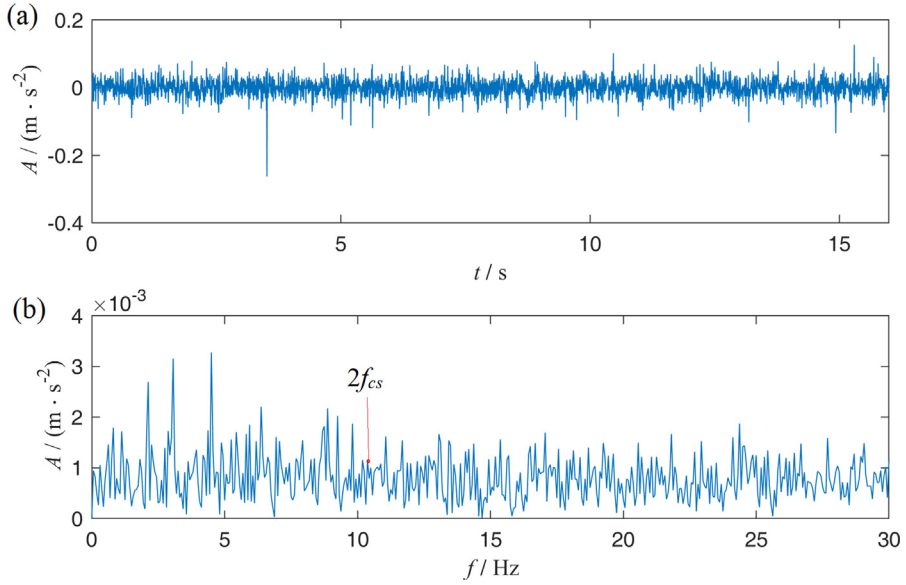


Fig. 31. Detection result of a planetary gearbox vibration signal with broken tooth fault obtained using the SE infogram method: (a) time-domain waveform and (b) envelope spectrum.

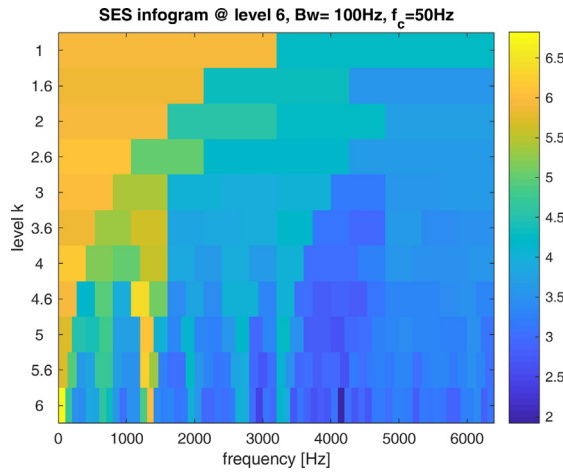


Fig. 32. SES infogram of a planetary gearbox vibration signal with broken tooth fault.

5.3. Fault diagnosis of broken tooth

As the severity of gear pitting increases, a broken tooth fault may occur. The faulty feature will then become more apparent compared with the micropitting fault. The same DDS test rig was used for the experiment on broken tooth fault diagnosis, and a broken tooth of the sun gear in the second stage was fabricated. In this experiment, the input rotational speed was also set as 2440 rpm, and the distributed fault characteristic frequency f_{cs} was also equal to 5.2 Hz due to the same parameters of the experimental planetary gearbox. The vibration signal was acquired using an accelerometer in the case of the planetary gearbox, and sampling frequency was 12800 Hz. The time-domain waveform, Fourier frequency spectrum, and envelope spectrum of the acquired signal are illustrated in Fig. 24(a), (b), and (c), respectively. Fig. 24(c) shows that the spectral peak at f_{cs} is apparent but does not have the largest amplitude. Furthermore, the spectral peak at $2f_{cs}$ is small. The proposed wavelets in Example 2 were applied to analyze this signal. Similarly, four-stage flexible wavelet transform was performed, and the wavelet coefficients were obtained, as shown in Fig. 25. The corresponding spectral negentropies are illustrated in Fig. 26. The best sub-band signal was obtained by the wavelet coefficient c_2^1 of the third channel in the first stage. Its time-domain waveform and envelope spectrum are shown in Fig. 27. This figure presents two apparent spectral

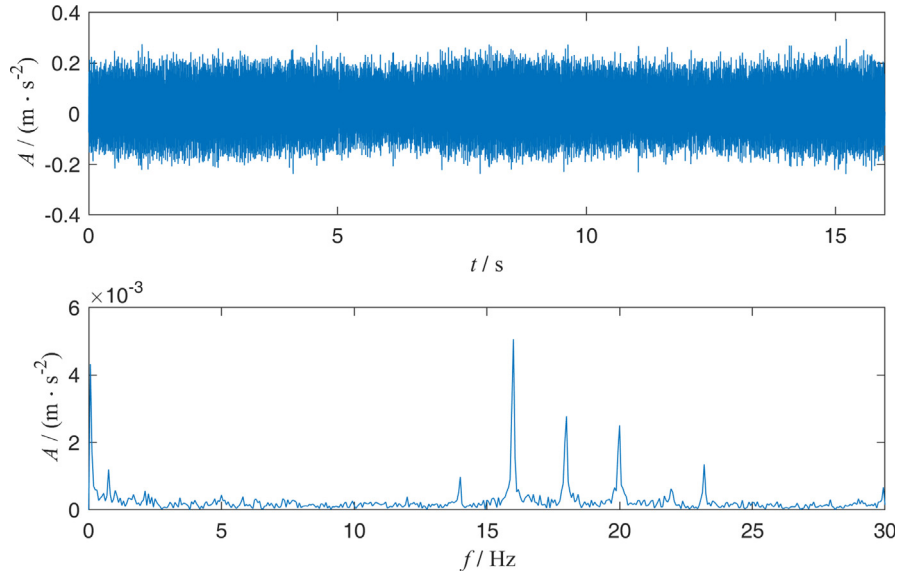


Fig. 33. Detection result of a planetary gearbox vibration signal with broken tooth fault obtained using the SES infogram method: (a) time-domain waveform and (b) envelope spectrum.

Table 2

Configuration parameters of the two-stage wind turbine planetary gearbox.

Level	Tooth number of sun gear	Tooth number of planet gear	Tooth number of ring gear	Number of planet gears
First stage	38	28	94	3
Second stage	71	31	134	3

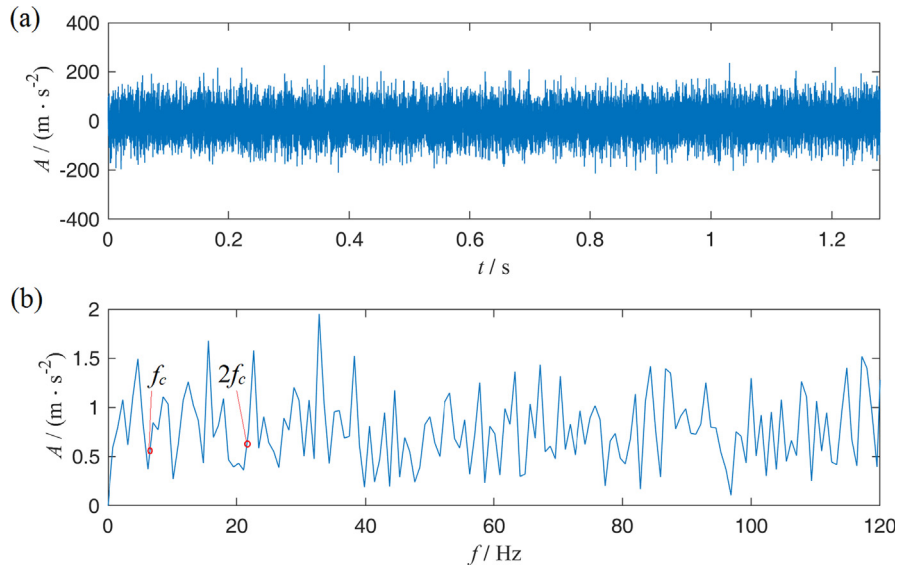


Fig. 34. Time-domain waveform and envelope spectrum of a faulty wind turbine planetary gearbox vibration signal: (a) time-domain waveform and (b) envelope spectrum.

peaks at f_{cs} and $2f_{cs}$, and the spectral line at f_{cs} has the largest amplitude. The sun gear in the second stage has a fault. Therefore, the effectiveness of the proposed method for the fault diagnosis of planetary gear transmission systems is validated.

Then, analytic wavelet transform, Morlet wavelet transform, SE infogram, and SES infogram were used for comparison. The characteristic component obtained via analytic wavelet transform and its envelope spectra are illustrated in Fig. 28.

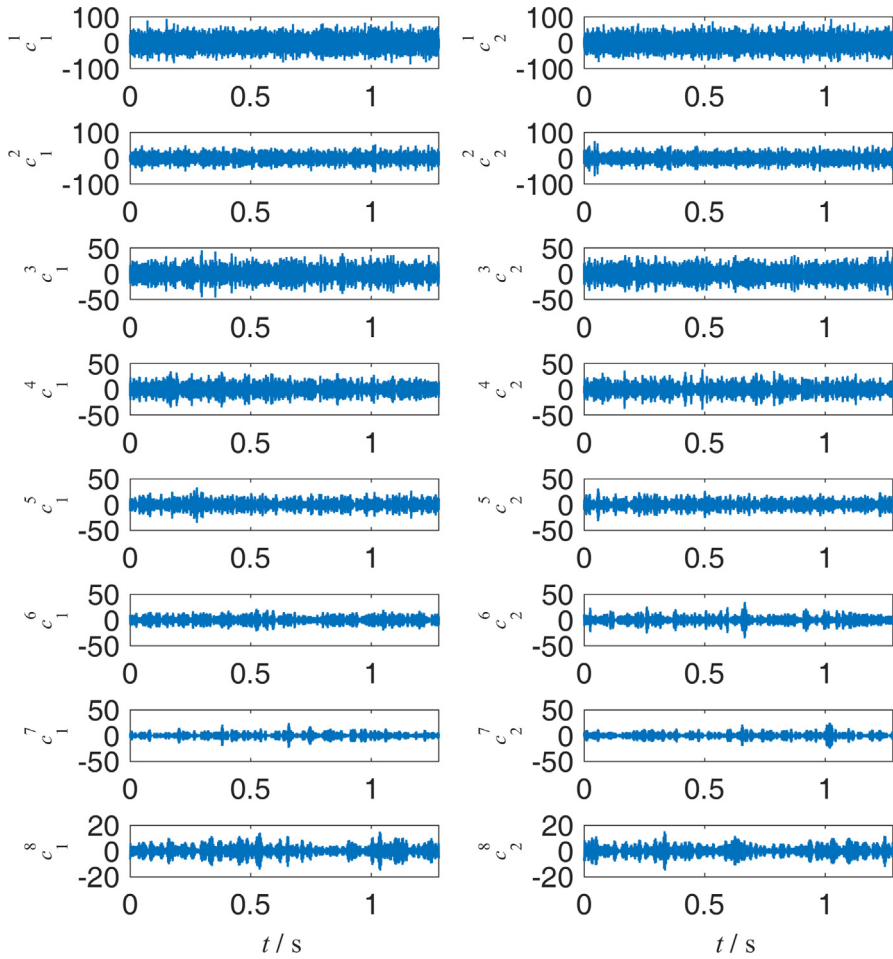


Fig. 35. Obtained wavelet coefficients of a faulty wind turbine planetary gearbox vibration signal.

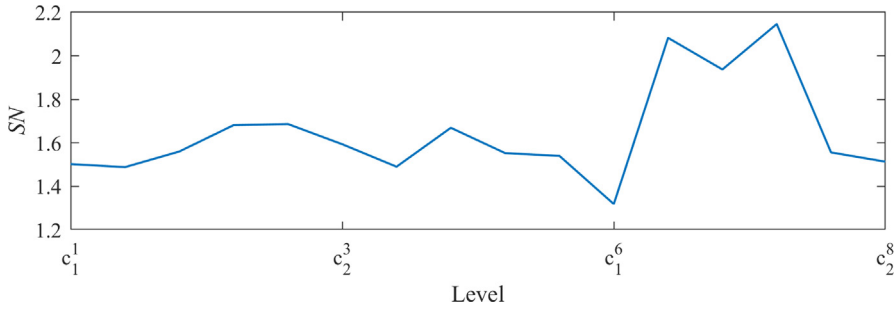


Fig. 36. Spectral negentropies of the wavelet coefficients of a faulty wind turbine planetary gearbox vibration signal.

The spectral peak at f_{cs} is apparent, whereas that at $2f_{cs}$ is not outstanding. With optimized Morlet wavelet transform, the obtained characteristic component and its envelope spectra are illustrated in Fig. 29. Although the spectral peak at f_{cs} is clear, its amplitude is not the largest. Moreover, the spectral peak at $2f_{cs}$ is relatively small. A comparison of Fig. 27 with Figs. 28 and 29 shows that the proposed transform exhibits better performance in transient feature extraction than traditional wavelet transforms. The filter parameters obtained using the average infogram were approximate to those obtained using the SE infogram or SES infogram, and thus, we did not use the average infogram for comparison to save space. First, the SE infogram of the vibration signal with broken tooth fault was calculated as shown in Fig. 30. On the basis of the optimal filter parameters listed in Fig. 30, the characteristic component was extracted, and their envelope spectra were calculated via Hilbert transform and Fourier transform. The time-domain waveform and envelope spectrum of the characteristic component are

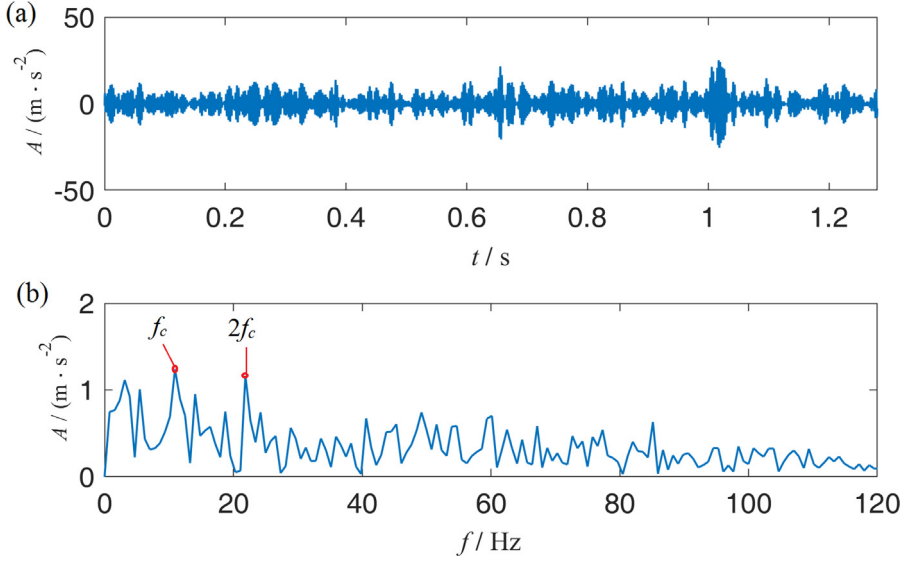


Fig. 37. Detection result of a faulty wind turbine planetary gearbox vibration signal obtained using the proposed method: (a) time-domain waveform and (b) envelope spectrum.

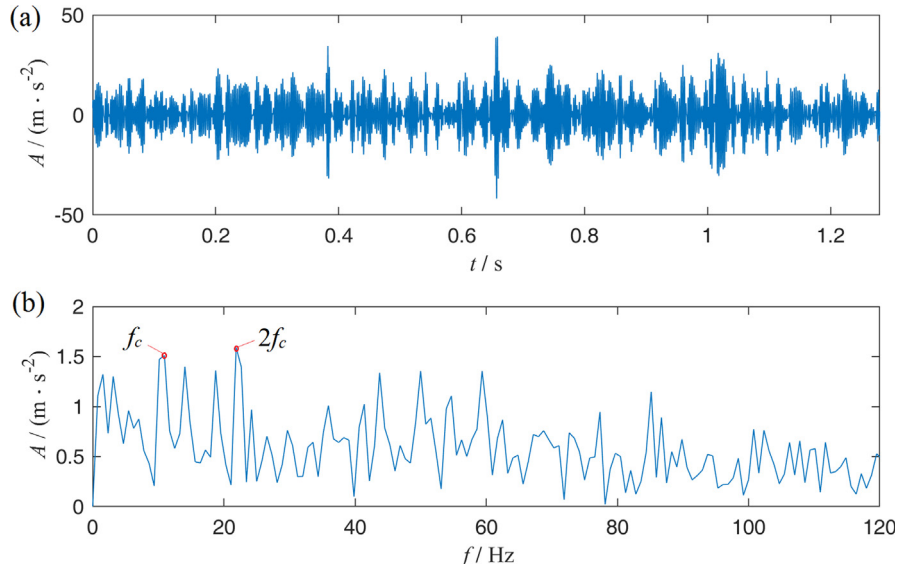


Fig. 38. Detection result of a faulty wind turbine planetary gearbox vibration signal obtained using the diagnosis method based on analytic wavelet transform: (a) time-domain waveform and (b) envelope spectrum.

presented in Fig. 31(a) and (b), respectively. Fig. 31(b) shows a small spectral peak at $2f_{cs}$. Second, the SES infogram was calculated as shown in Fig. 32. In accordance with the optimal filter parameters given in Fig. 32, the characteristic component and its envelope spectrum were obtained as shown in Fig. 33. No spectral peak was observed at the fault characteristic frequency and its multiplication. Detecting the sun gear fault from Figs. 31 and 33 is difficult. The preceding comparative results demonstrate the superiority of the proposed M-band flexible wavelet transform over other typical decomposition methods.

5.4. Fault diagnosis of a wind turbine gearbox

As the key component of a wind turbine, a planetary gearbox easily suffers from fault due to its complex working condition. To ensure the safety of a wind turbine, the fault in a planetary gearbox must be detected. However, the fault feature may be submerged in background noise and normal vibration components. Thus, diagnosing the glitch of a planetary gearbox using traditional methods, such as Fourier spectrum, cepstrum, and Hilbert envelope spectrum, is not easy and robust.

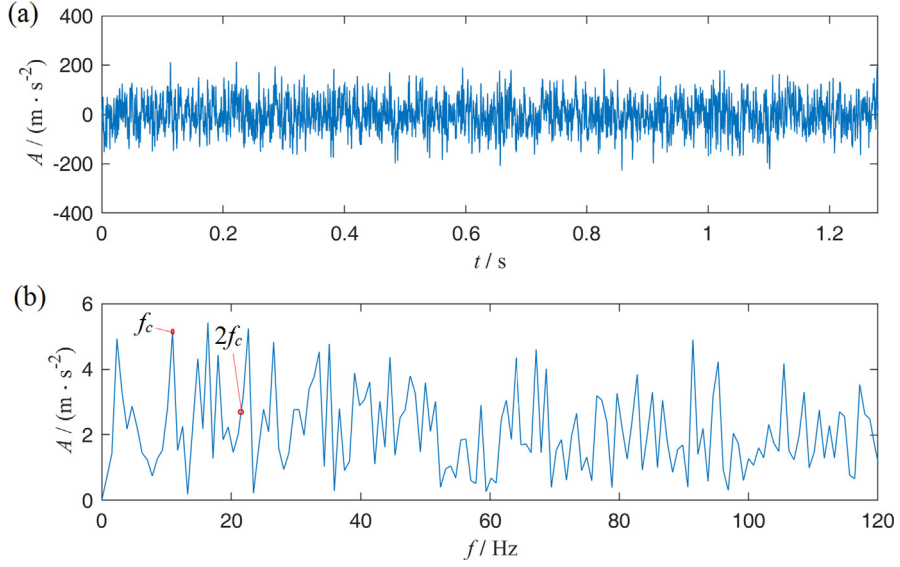


Fig. 39. Detection result of a faulty wind turbine planetary gearbox vibration signal obtained using the diagnosis method based on Morlet wavelet transform: (a) time-domain waveform and (b) envelope spectrum.

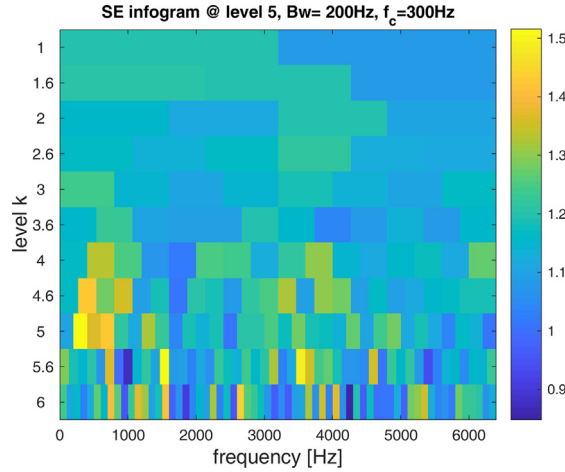


Fig. 40. SE infogram of a faulty wind turbine planetary gearbox vibration signal.

Therefore, the proposed fault diagnosis method was used to extract the weak fault feature to demonstrate the effectiveness and advantage of the M-band flexible wavelet transform.

A fault diagnosis experiment on a wind turbine planetary gearbox was performed. The tested two-stage wind turbine planetary gearbox had a minor fault in the output sun gear, and its configuration parameters are listed in Table 2. An accelerometer was placed on the case of the planetary gearbox to acquire the vibration signal, and the sampling frequency was set as 12800 Hz. The input rotational speed and the output rotational speed were set as 101 rpm and 1018 rpm, respectively. In accordance with the structure parameter and working condition, the fault characteristic frequency f_c was calculated as 10.94 Hz. The time-domain waveform of the vibration signal is illustrated in Fig. 34(a). Through conventional Hilbert envelope spectrum analysis, the envelope spectrum of the faulty vibration signal is shown in Fig. 34(b). Clear spectral peaks are not observed at the fault characteristic frequency and its frequency multiple (marked with red circles in the figure). The proposed method was used to detect the fault. The obtained wavelet coefficients after eight-stage decomposition are shown in Fig. 35, and the corresponding spectral negentropies are shown in Fig. 36. The optimal characteristic component was obtained using the wavelet coefficient c_2^7 of the third channel in the seventh stage, and its time-domain waveform and envelope spectrum are presented in Fig. 37(a) and (b), respectively. Fig. 37(b) shows distinct spectral peaks at f_c and $2f_c$ and the output sun gear's fault.

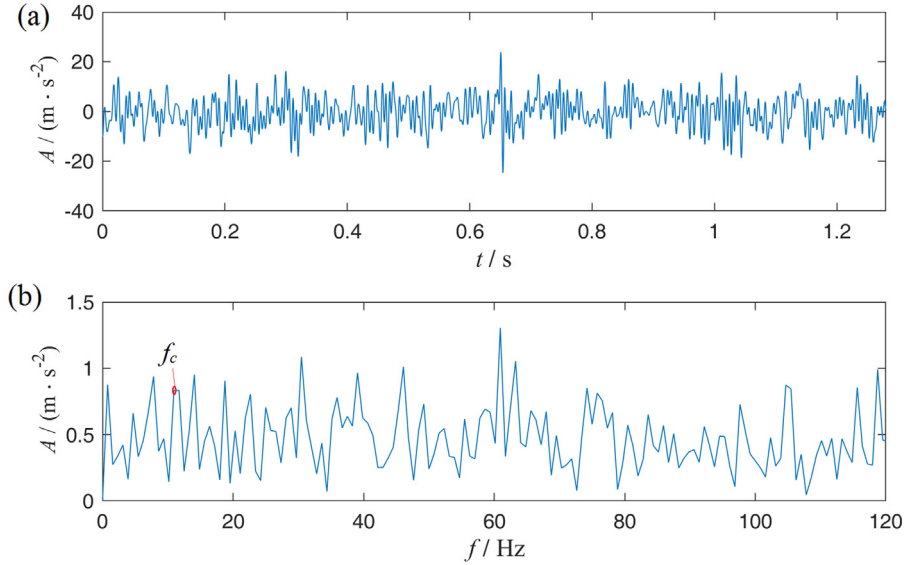


Fig. 41. Detection result of a faulty wind turbine planetary gearbox vibration signal obtained using the SE infogram method: (a) time-domain waveform and (b) envelope spectrum.

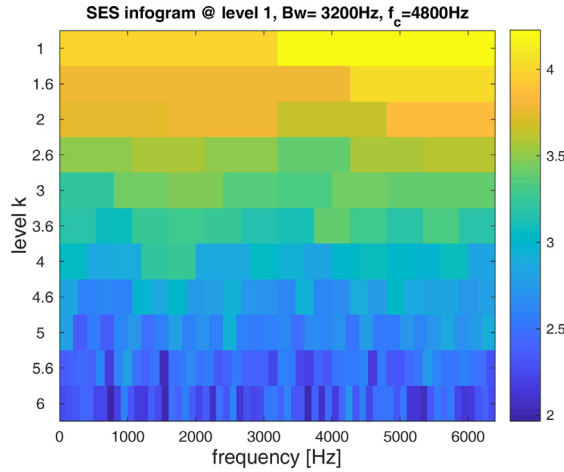


Fig. 42. SES infogram of a faulty wind turbine planetary gearbox vibration signal.

Similarly, the proposed method was compared with analytic wavelet transform, Morlet wavelet transform, SE infogram, and SES infogram. First, the characteristic component and its envelope spectrum obtained using the fault diagnosis method based on analytic wavelet transform are illustrated in Fig. 38(a) and (b), respectively. Two clear spectral peaks are observed at f_c and $2f_c$, but the amplitude at f_c is smaller than that at $2f_c$. Second, using optimized Morlet wavelet transform, the characteristic component was obtained and its envelope spectrum was calculated. The time-domain waveform and envelope spectrum of the characteristic component are illustrated in Fig. 39(a) and (b), respectively. Fig. 39(b) shows a spectral peak at f_c , but its amplitude is not the largest; no spectral peak is observed at $2f_c$ and other frequency multiplications. By comparing Fig. 37(b) with Fig. 38(b) and 39(b), we can conclude that the proposed M-band flexible wavelet transform can better extract fault feature than analytic wavelet transform and Morlet wavelet transform due to its higher time–frequency sampling density. Third, the SE infogram of the faulty wind turbine planetary gearbox vibration signal was calculated, and the results are presented in Fig. 40. Given the optimal filter parameters, we extracted the characteristic component and calculated its envelope spectrum as shown in Fig. 41. Only an unclear spectral peak is observed at the fault characteristic frequency f_c . Lastly, the SES infogram was calculated as shown in Fig. 42. In accordance with the optimal filter parameters list in Fig. 42, the characteristic component and its envelope spectrum were obtained as illustrated in Fig. 43(a) and (b), respectively. A spectral peak is observed at f_c , but its amplitude is not the largest. Figs. 41 and 43 show that we barely deter-

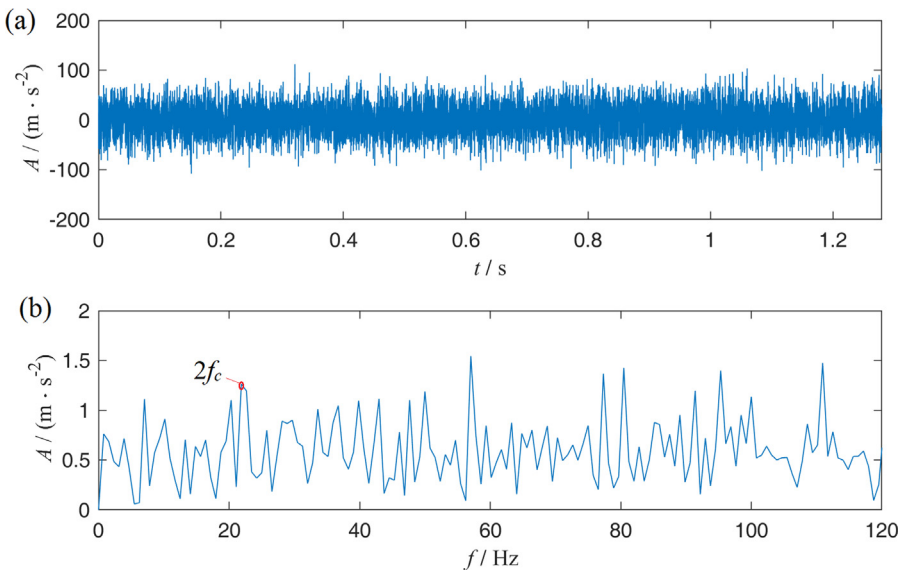


Fig. 43. Detection result of a faulty wind turbine planetary gearbox vibration signal obtained using the SES infogram method: (a) time-domain waveform and (b) envelope spectrum.

mine whether a fault exists in the output sun gear using the two infogram methods. Therefore, the preceding comparative results indicate that the proposed fault diagnosis method based on M-band flexible wavelet transform is superior to the fault diagnosis methods based on analytic wavelet transform, Morlet wavelet transform, the SE infogram, and the SES infogram.

6. Conclusions

The major contribution of this study is the newly constructed M-band flexible wavelet transform. Its filter bank has three channels, namely, a low-pass filtering channel, a band-pass filtering channel, and a high-pass filtering channel. These channels lead to a high time–frequency sampling density. Moreover, the filter parameters and dilation factors can be easily specified. A perfect reconstruction condition of the proposed transform was established. In accordance with this condition, the filter bank was designed using a frequency-domain method. Its numerical implementation algorithm was explored on the basis of the equivalent filter bank and discrete Fourier transform. Several wavelet construction examples of the proposed M-band flexible wavelet transform were presented. Compared with analytic wavelet transform, orthogonal wavelet transform, and biorthogonal wavelet transform, the proposed wavelet transform achieves better denoising performance, particularly when the threshold is small. Lastly, by using M-band flexible wavelet transform and spectral negentropy, a fault diagnosis method for planetary transmission systems was developed. The performance of this method was validated via three fault diagnosis experiments. The comparative results indicate that the proposed fault diagnosis method can more effectively detect the faults of planetary gear transmission systems than the fault diagnosis methods based on analytic wavelet transform, Morlet wavelet transform, and infograms.

An extension of this work is to research the application of the proposed wavelet basis to sparse representation. Determining how to add more band-pass filtering channels to further improve time–frequency covering and how to optimize wavelet parameters using a genetic algorithm or the particle swarm algorithm can also be studied in the future.

Acknowledgments

The work described in this paper was supported by the National Natural Science Foundation of China (no. 51675065), Chongqing Research Program of Basic Research and Frontier Technology (no. cstc2017jcyjAX0459) and the Fundamental Research Funds for the Central Universities (no. 2018CDQYJX0011 and 2018CDJD0001).

References

- [1] Y. Lei, J. Lin, M.J. Zuo, Z. He, Condition monitoring and fault diagnosis of planetary gear transmission systems: a review, *Measurement* 48 (2014) 292–305.
- [2] M. Zhao, X. Jia, J. Lin, Y. Lei, J. Lee, Instantaneous speed jitter detection via encoder signal and its application for the diagnosis of planetary gearbox, *Mech. Syst. Signal Process.* 98 (2018) 16–31.

- [3] F. Chaari, T. Fakhfakh, M. Haddar, Analytical investigation on the effect of gear teeth faults on the dynamic response of a planetary gear set, *Noise Vibration Worldwide* 37 (2009) 9–15.
- [4] J. Parra, C.M. Vicuña, Two methods for modeling vibrations of planetary gear transmission systems including faults: comparison and validation, *Mech. Syst. Signal Process.* 92 (2017) 213–225.
- [5] J.R. Ottewill, M. Orkisz, Condition monitoring of gearboxes using synchronously average delectric motor signals, *Mech. Syst. Signal Process.* 38 (2013) 482–498.
- [6] A. Saxena, B.Q. Wu, G. Vachtsevanos, A methodology for analyzing vibration data from planetary gear systems using complex Morlet wavelets, in: 2005 American Control Conference, Portland, OR, USA, June 8–10, 2005, pp. 4730–4735.
- [7] Y. Qin, J.X. Wang, Y.F. Mao, Dense framelets with two generators and their application in mechanical fault diagnosis, *Mech. Syst. Signal Process.* 40 (2) (2013) 483–498.
- [8] W.D. Mark, H. Lee, R. Patrick, et al, A simple frequency-domain algorithm for early detection of damaged gear teeth, *Mech. Syst. Signal Process.* 24 (2010) 2807–2823.
- [9] M. Zhang, K. Wang, D. Wei, M.J. Zuo, Amplitudes of characteristic frequencies for fault diagnosis of planetary gearbox, *J. Sound Vib.* 432 (2018) 119–132.
- [10] X. Chen, Z. Feng, Iterative generalized time–frequency reassignment for planetary gearbox fault diagnosis under nonstationary conditions, *Mech. Syst. Signal Process.* 80 (2016) 429–444.
- [11] Z.P. Feng, M. Liang, Y. Zhang, et al, Fault diagnosis for wind turbine planetary gear transmission systems via demodulation analysis based on ensemble empirical mode decomposition and energy separation, *Renew. Energy* 47 (2012) 112–126.
- [12] Z. Feng, S. Qin, M. Liang, Time–frequency analysis based on Vold–Kalman filter and higher order energy separation for fault diagnosis of wind turbine planetary gearbox under nonstationary conditions, *Renew. Energy* 85 (2016) 45–56.
- [13] G. He, K. Ding, W. Li, X. Jiao, A novel order tracking method for wind turbine planetary gearbox vibration analysis based on discrete spectrum correction technique, *Renew. Energy* 87 (Part 1) (2016) 364–375.
- [14] Z. Du, X. Chen, et al, Sparse feature identification based on union of redundant dictionary for wind turbine gearbox fault diagnosis, *IEEE Trans. Ind. Electron.* 62 (10) (2015) 6594–6605.
- [15] Y. Qin, J. Zou, F. Cao, Adaptively detecting the transient feature of faulty wind turbine planetary gear transmission systems by the improved kurtosis and iterative thresholding algorithm, *IEEE Access* 6 (2018) 14602–14612.
- [16] Y. Li, G. Li, Y. Yang, X. Liang, M. Xu, A fault diagnosis scheme for planetary gear transmission systems using adaptive multi-scale morphology filter and modified hierarchical permutation entropy, *Mech. Syst. Signal Process.* 105 (2018) 319–337.
- [17] Y. Li, Y. Yang, G. Li, M. Xu, W. Huang, A fault diagnosis scheme for planetary gear transmission systems using modified multi-scale symbolic dynamic entropy and mRMR feature selection, *Mech. Syst. Signal Process.* 91 (2017) 295–312.
- [18] T. Barszcz, R.B. Randall, Application of spectral kurtosis for detection of a tooth crack in the planetary gear of a wind turbine, *Mech. Syst. Signal Process.* 23 (2009) 1352–1365.
- [19] Y. Qin, X. Wang, J. Zou, The optimized deep belief networks with improved logistic Sigmoid units and their application in fault diagnosis for planetary gear transmission systems of wind turbines, *IEEE Trans. Ind. Electron.* 66 (5) (2019) 3814–3824.
- [20] Z. Feng, M.J. Zuo, J. Qu, T. Tian, Z. Liu, Joint amplitude and frequency demodulation analysis based on local mean decomposition for fault diagnosis of planetary gear transmission systems, *Mech. Syst. Signal Process.* 40 (1) (2013) 56–75.
- [21] Y. Lei, Z. Liu, X. Wu, N. Li, W. Chen, J. Lin, Health condition identification of multi-stage planetary gear transmission systems using a mRVM-based method, *Mech. Syst. Signal Process.* 60 (2015) 289–300.
- [22] J. Qu, Z. Liu, M.J. Zuo, H.-Z. Huang, Feature selection for damage degree classification of planetary gear transmission systems using support vector machine, *Proc. Inst. Mech. Eng. Part C J. Mech. Eng. Sci.* 225 (9) (2011) 2250–2264.
- [23] Z. Cheng, N. Hu, X. Zhang, Crack level estimation approach for planetary gearbox based on simulation signal and GRA, *J. Sound Vib.* 331 (26) (2012) 5853–5863.
- [24] D.M. Blunt, J.A. Keller, Detection of a fatigue crack in a UH-60A planet gear carrier using vibration analysis, *Mech. Syst. Signal Process.* 20 (8) (2006) 2095–2111.
- [25] J. Yoon, D. He, B. Van Hecke, T.J. Nostrand, J. Zhu, E. Bechhoefer, Vibration-based wind turbine planetary gearbox fault diagnosis using spectral averaging, *Wind Energy* 19 (2016) 1733–1747.
- [26] R. Zimroz, A. Bartkowiak, Two simple multivariate procedures for monitoring planetary gear transmission systems in non-stationary operating conditions, *Mech. Syst. Signal Process.* 38 (1) (2013) 237–247.
- [27] I. Antoniadou, G. Manson, W.J. Staszewski, T. Barszcz, K. Worden, A time–frequency analysis approach for condition monitoring of a wind turbine gearbox under varying load conditions, *Mech. Syst. Signal Process.* 64–65 (2015) 188–216.
- [28] W. Sweldens, The lifting scheme: a custom-design construction of biorthogonal wavelets, *Appl. Comput. Harmon. Anal.* 3 (2) (1996) 186–200.
- [29] P.D. Samuel, D.J. Pines, Constrained adaptive lifting and the CAL4 metric for helicopter transmission diagnostics, *J. Sound Vib.* 319 (2009) 698–718.
- [30] H. Sun, Y. Zi, Z. He, et al, Customized Multiwavelets for planetary gearbox fault detection based on vibration sensor signals, *Sensors* 13 (1) (2013) 1183–1209.
- [31] I. Daubechies, B. Han, A. Ron, Z. Shen, Framelets: MRA-based constructions of wavelet frames, *Appl. Comput. Harmon. Anal.* 14 (1) (2003) 1–46.
- [32] B. Dong, Z.W. Shen, Pseudo-splines, wavelets and framelets, *Appl. Comput. Harmon. Anal.* 22 (1) (2007) 78–104.
- [33] I.W. Selesnick, The double density DWT, in: A. Petrosian, F.G. Meyer (Eds.), *Wavelets in Signal and Image Analysis: From Theory to Practice*, Kluwer Academic, 2001.
- [34] Y. Qin, B.P. Tang, J.X. Wang, Higher-density dyadic wavelet transform and its application, *Mech. Syst. Signal Process.* 24 (3) (2010) 823–834.
- [35] T. Blu, Iterated filter banks with rational rate changes–connection with discrete wavelet transforms, *IEEE Trans. Signal Process.* 41 (12) (1993) 3232–3244.
- [36] I. Bayram, I.W. Selesnick, Frequency-domain design of overcomplete rational-dilation wavelet transforms, *IEEE Trans. Signal Process.* 57 (8) (2009) 2957–2972.
- [37] B. Chen, Z. Zhang, C. Sun, et al, Fault feature extraction of gearbox by using overcomplete rational dilation discrete wavelet transform on signals measured from vibration sensors, *Mech. Syst. Signal Process.* 33 (2012) 275–298.
- [38] I. Bayram, An analytic wavelet transform with a flexible time–frequency covering, *IEEE Trans. Signal Process.* 61 (2013) 1131–1142.
- [39] C.L. Zhang, B. Li, B.Q. Chen, H.R. Cao, Y.Y. Zi, Z.J. He, Weak fault signature extraction of rotating machinery using flexible analytic wavelet transform, *Mech. Syst. Signal Process.* 64–65 (2015) 162–187.
- [40] J. Antoni, The infogram: Entropic evidence of the signature of repetitive transients, *Mech. Syst. Signal Process.* 74 (2016) 73–94.
- [41] P.P. Vaidyanathan, *Multirate Systems and Filter Banks*, Englewood Cliffs, Prentice-Hall, NJ, 1992.
- [42] I.W. Selesnick, Wavelet transform with tunable Q-factor, *IEEE Trans. Signal Process.* 59 (8) (2009) 3560–3575.
- [43] I. Daubechies, *Ten Lectures on Wavelets*, Philadelphia, SIAM, PA, 1992.
- [44] Y. Qin, A new family of model-based impulsive wavelets and their sparse representation for rolling bearing fault diagnosis, *IEEE Trans. Ind. Electron.* 65 (2018) 2716–2726.